Astronomy & Astrophysics

Large Interferometer For Exoplanets (LIFE)

XIV. Finding terrestrial protoplanets in the galactic neighborhood

Lorenzo Cesario[1,*], Tim Lichtenberg[1,*], Eleonora Alei[2], Óscar Carrión-González[3], Felix A. Dannert[4,5,18], Denis Defrère[6], Steve Ertel[7,8], Andrea Fortier[9,18], A. García Muñoz[10], Adrian M. Glauser[4], Jonah T. Hansen[4,5], Ravit Helled[11], Philipp A. Huber[4], Michael J. Ireland[12], Jens Kammerer[13], Romain Laugier[6], Jorge Lillo-Box[14], Franziska Menti[4], Michael R. Meyer[15], Lena Noack[16], Sascha P. Quanz[4,17,5], Andreas Quirrenbach[19], Sarah Rugheimer[20], Floris van der Tak[21], Haiyang S. Wang[4,22,23], Marius Anger[24], Olga Balsalobre-Ruza[14], Surendra Bhattarai[25], Marrick Braam[6,26,27], Amadeo Castro-González[14], Charles S. Cockell[28], Tereza Constantinou[29], Gabriele Cugno[30], Jeanne Davoult[31], Manuel Güdel[32], Nina Hernitschek[33], Sasha Hinkley[34], Satoshi Itoh[35], Markus Janson[36], Anders Johansen[37], Hugh R. A. Jones[38], Stephen R. Kane[39], Tim A. van Kempen[47], Kristina G. Kislyakova[32], Judith Korth[40], Andjelka B. Kovačević[41], Stefan Kraus[42], Rolf Kuiper[43], Joice Mathew[44], Taro Matsuo[45], Yamila Miguel[46], Michiel Min[47], Ramon Navarro[48], Ramses M. Ramirez[49], Heike Rauer[50], Berke Vow Ricketti[51,52], Amedeo Romagnolo[53], Martin Schlecker[54], Evan L. Sneed[39], Vito Squicciarini[3,55], Keivan G. Stassun[56], Motohide Tamura[35], Daniel Viudez-Moreiras[14], Robin D. Wordsworth[57], and the LIFE Collaboration[**]

(Affiliations can be found after the references)

ABSTRACT

Context. The increased brightness temperature of young rocky protoplanets during their magma ocean epoch makes them potentially amenable to atmospheric characterization at distances from the Solar System far greater than thermally equilibrated terrestrial exoplanets, offering observational opportunities for unique insights into the origin of secondary atmospheres and the near surface conditions of prebiotic environments.

Aims. The Large Interferometer For Exoplanets (LIFE) mission will employ a space-based midinfrared nulling interferometer to directly measure the thermal emission of terrestrial exoplanets. In this work, we seek to assess the capabilities of various instrumental design choices of the LIFE mission concept for the detection of cooling protoplanets with transient high-temperature magma ocean atmospheres at the tail end of planetary accretion. In particular, we investigate the minimum integration times necessary to detect transient magma ocean exoplanets in young stellar associations in the Solar neighborhood.

Methods. Using the LIFE mission instrument simulator (LIFEsim), we assessed how specific instrumental parameters and design choices, such as wavelength coverage, aperture diameter, and photon throughput, facilitate or disadvantage the detection of protoplanets. We focused on the observational sensitivities of distance to the observed planetary system, protoplanet brightness temperature (using a blackbody assumption), and orbital distance of the potential protoplanets around both G- and M-dwarf stars.

Results. Our simulations suggest that LIFE will be able to detect ($S/N \geq 7$) hot protoplanets in young stellar associations up to distances of 100 pc from the Solar System for reasonable integration times (up to a few hours). Detection of an Earth-sized protoplanet orbiting a Solar-sized host star at 1 AU requires less than 30 minutes of integration time. M-dwarfs generally need shorter integration times. The contribution from wavelength regions smaller than 6 µm is important for decreasing the detection threshold and discriminating emission temperatures.

Conclusions. The LIFE mission is capable of detecting cooling terrestrial protoplanets within minutes to hours in several local young stellar associations hosting potential targets. The anticipated compositional range of magma ocean atmospheres motivates further architectural design studies to characterize the crucial transition from primary to secondary atmospheres.

Key words. instrumentation: interferometers – planets and satellites: detection – planets and satellites: terrestrial planets

1. Introduction

The Large Interferometer For Exoplanets (LIFE) Collaboration (LIFE-space-mission.com) is developing the roadmap for the technical implementation and scientific exploitation of a space-based midinfrared nulling interferometer that can detect and characterize terrestrial exoplanets (Quanz et al. 2022a,b). Previous studies have shown promising simulation results for exoplanet detection and characterization focused on cool, potentially habitable exoplanets (Dannert et al. 2022; Konrad et al. 2022, 2023; Alei et al. 2022; Kammerer et al. 2022; Hansen et al. 2022, 2023; Angerhausen et al. 2023, 2024; Carrión-González et al. 2023; Kammerer & Quanz 2018), with possible variations in architectural and instrumentation design influencing the

* Corresponding authors; l.cesario@rug.nl,
tim.lichtenberg@rug.nl
** LIFE-space-mission.com

accessible parameter space (Hansen et al. 2022, 2023; Matsuo et al. 2023). So far, only a few studies have considered the extensive potential of the LIFE concept on questions surrounding the formation and evolution of planetary systems (Bonati et al. 2019; Janson et al. 2023).

In this paper, we focused on the potential of finding terrestrial protoplanets in their early transient magma ocean phase following planetary accretion, when rocky planets are globally molten rather than solid. Highly molten magma ocean phases are a standard outcome of planetary formation (Chao et al. 2021; Lichtenberg et al. 2023) since both planetesimal-based models (e.g., Alibert et al. 2013; Quintana et al. 2016; Wyatt et al. 2019; Emsenhuber et al. 2021; Schlecker et al. 2021a,b; Clement et al. 2020, 2022; Lichtenberg & Clement 2022) and pebble accretion models (e.g., Morbidelli & Nesvorny 2012; Lambrechts et al. 2019; Johansen et al. 2021, 2023; Olson et al. 2022; Olson & Sharp 2023) predict a phase of high-energy impacts. This phase of planetary evolution is of crucial importance for the transition between the primary and secondary atmosphere, as during highly molten phases the distribution of atmospheric volatiles between the planetary metal core, the silicate mantle, and the volatile envelope is established (Lichtenberg et al. 2023; Krijt et al. 2023; Suer et al. 2023).

Rather than solely mature secondary atmospheres of terrestrial exoplanets, we also need to observationally characterize magma ocean epochs for a better understanding of planetary evolution. Earth-sized planets with secondary atmospheres are typically thought to host oxidizing planetary mantles due to the pressure sensitivity of internal geochemical reactions (Armstrong et al. 2019; Gaillard et al. 2021; Hirschmann 2022, 2023), which means their volcanic emissions would be rich in gasses such as CO_2, H_2O, and SO_2, influencing long-term climatic and surface conditions. However, whether the prebiotic climate on Earth at the transition between the primary and secondary atmosphere was equally oxidizing is an ongoing enigma (Zahnle & Carlson 2020; Catling & Zahnle 2020). Yet, it is crucially important for the chemical synthesis of surficial life (Sasselov et al. 2020; Benner et al. 2020). Placing temporal constraints on the transition of a planet from a primary atmosphere to a secondary atmosphere, and potentially its surface temperature regime, will allow for a better understanding of when the surface of early Earth (and other terrestrial rocky planets) became suitable for life as we know it. If one was to take the upper temperature limit of life to be 122°C (Takai et al. 2008), observations from LIFE will allow for a better estimate of the time between accretion and surface conditions suitable for life. Furthermore, the study of early atmospheric transitions will shed light on the early surface chemical conditions for life, including the redox state and the atmospheric gases available for metabolism. This will elucidate the physical and chemical conditions in which life emerges after accretion and the chemical inventory of molecules available to a potential biosphere in the earliest stages of its emergence (Cockell et al. 2023).

At least part of the answer to the chemical nature of the volatile envelope at this transitional stage lies in the chemical segregation that occurs during the magma ocean epoch (Suer et al. 2023; Lichtenberg & Miguel 2024). During these highly molten episodes, the chemical transfer of atmospheric volatiles between core, mantle, and atmosphere is rapid due to hour- to day-long convection timescales in planetary magma oceans (Solomatov 2015). Vigorous convection in magma oceans diffuses the boundary between the metallic core and the silicate mantle (Lichtenberg 2021), which affects the composition of the outgassed atmosphere (Schlichting & Young 2022). Dissolution

of volatiles, such as water, into the magma ocean, and loss to space further alters the chemical composition of the magma ocean atmosphere (Schaefer et al. 2016; Lichtenberg et al. 2021; Dorn & Lichtenberg 2021; Bower et al. 2022). Therefore, being able to study the composition of magma atmospheres in extrasolar planetary systems would substantially aid in interpreting the scarce geologic record of the prebiotic Earth, and potentially improve the general understanding of the conditions that enabled the origin of life as we know it (Sleep et al. 2001; Zahnle & Carlson 2020). In addition, valuable insights could be gained into the potential abundance of reduced exoplanet climates with variable greenhouse forcing and thus liquid water stability (Pierrehumbert & Gaidos 2011; Ramirez & Kaltenegger 2017).

Furthermore, the study of terrestrial planets during their magma ocean phase will provide critical insight regarding the eventual pathway of volatile inventories, most particularly water content. Hamano et al. (2013) showed that the duration of the magma phase for terrestrial planets can determine whether water is able to condense on the surface and form oceans, or remain in the atmosphere as a greenhouse gas. Indeed, the climate simulations of Turbet et al. (2021) demonstrate the possibility that water remaining in the atmosphere can migrate to the night side of the planet, warming the surface further and preventing the ocean formation, possibly explaining the evolutionary pathway of Venus relative to Earth (Kane et al. 2019). Alternatively, if water oceans were able to form on an early Venus, then cloud formation at the substellar point may have allowed temperate conditions to remain for several billion years (Way & Del Genio 2020). The resolution of these various scenarios will be critically important in a proper evaluation of terrestrial exoplanets found within the Venus Zone of their stars (Kane et al. 2014; Ostberg et al. 2023) and understanding their evolutionary pathways.

The LIFE mission can also shed light on another important feature of planetary evolution, namely, the presence and influence of the primordial envelope. During the first few million years, the environment around a star is dominated by a protoplanetary disk of gas and dust, often referred to as the solar nebula, in which the planets form. Disks likely survive 2–10 Myr (Mamajek 2009). Within the disk, a planet of sufficient mass can accrete a primordial envelope from the disk (Stökl et al. 2015; Owen & Mohanty 2016; Lammer et al. 2020). How rapidly this envelope is then lost depends on the evolution of the young star. Some components of this primordial envelope might still be present in the modern Earth after having been dissolved in the molten mantle (Williams & Mukhopadhyay 2019). Contribution from this primordial envelope might influence the magma ocean composition and the observational fingerprints of the hot planets seen by LIFE.

Previous work on this stage of planetary evolution focuses on debris disks in exoplanetary systems and the detection of post-collision dust clouds as important circumstantial evidence of giant impacts at the tail end of planetary accretion (e.g., Wyatt et al. 2007; Löhne et al. 2008; Jackson & Wyatt 2012; Kral et al. 2018, 2020; Ertel et al. 2018; Thompson et al. 2019; Su et al. 2019; Gaidos et al. 2019, 2022; Defrère et al. 2021; Janson et al. 2023; Bonsor et al. 2023; Han et al. 2023; Kenworthy et al. 2023). Here, in contrast, we focused on the detection of the magma ocean surface or magma ocean atmosphere itself (Stern 1994; Zhang & Sigurdsson 2003; Mamajek & Meyer 2007; Miller-Ricci et al. 2009; Lupu et al. 2014; Hamano et al. 2015; Bonati et al. 2019). In the literature, this is sometimes called collision afterglow, with the giant impact of terrestrial planetary accretion in mind. Here, however, we are agnostic of

the physical nature of the heating event and solely focus on the potential for a significantly bright point source in exoplanetary systems in different observational circumstances. In general, magma ocean surfaces and atmospheres are assumed to be hot (1000–3000 K) and thus bright in the near and midinfrared (IR) (Elkins-Tanton 2012). However, with varying atmospheric composition, crystallization state over time (Lichtenberg et al. 2021; Graham et al. 2021), and steam-dominated protoplanets typically settling quickly onto the Simpson-Nakajima limit (the thermal emission threshold defining the inner edge of the classical habitable zone concept; e.g., Goldblatt et al. 2013; Goldblatt 2015; Boukrouche et al. 2021), the emission temperature of protoplanets could be several hundreds of Kelvin lower. Thus we are to consider protoplanets of a wide range of potential emission temperatures.

The work by Bonati et al. (2019) treated the observational prospects of LIFE's 5.6 μm and 10 μm filters to detect post-impact afterglows in nearby young stellar associations. In this paper, we considered different instrument parameters of the LIFE concept comprising wavelength ranges that extend from a minimum of 3 μm to 20 μm. We evaluated the relative performances and analyzed under which circumstances a cooling protoplanet can be detected by LIFE in a certain distance range and how much time these observations would require. Our goal is to study the instrument's capabilities and the possibility of detecting magma ocean protoplanets in young stellar associations.

2. Methods

2.1. Instrument setup and scenario

For performance estimations of the LIFE instrument in detecting hot protoplanets we used LIFE's mission simulator (LIFEsim) (Dannert et al. 2022), which simulates observations performed by the LIFE concept and allows parameter manipulation to study different instrumental setups. The LIFE simulator includes in its model the contribution of the major astrophysical noises, such as photon noise and dust emission from the local and exozodiacal disks. LIFEsim calculates each astrophysical noise term individually, these terms are then integrated over a two-dimensional artificial image. The distribution of exozodiacal dust is simulated according to the model by Kennedy et al. (2015). The dust emission model in LIFEsim assumes that its distribution is similar to the Solar System's. The emission is optically thin and LIFEsim approximates its (dimensionless) face-on surface density with a power law distribution (Dannert et al. 2022). The emission is then modeled as blackbody radiation from a face-on disk (temperature-radius profile). The disks are also assumed to always be face-on, symmetric and homogeneous. A study of the impact of angled disks on observations with LIFEsim can be found in Quanz et al. (2022b). LIFEsim does not yet include, however, instrumental noise. We handled this uncertainty by adding an educated guess of the potential instrumental noise range to our calculations, further discussed below.

For this paper, all but three instrument parameters were left to the default values from Quanz et al. (2022b), as summarized in Table 1. The set of these three parameters constitutes the observing scenario for LIFE of which three major variations were considered, termed the BASELINE, OPTIMISTIC and PESSIMISTIC scenarios. These scenarios were defined in Quanz et al. (2022b) and can be found in Table 2.

The aperture diameter greatly affects the detection yield of the interferometer, especially when dealing with smaller, mature,

Table 1. LIFEsim instrument setup and major parameters.

Parameter	Unit	Default
Aperture diameter	[m]	2
Minimum wavelength	[μm]	4
Maximum wavelength	[μm]	18.5
Quantum efficiency	[%]	70
Photon throughput	[%]	5
Spectral resolution		20
Minimum nulling length	[m]	10
Maximum nulling length	[m]	100
Imaging/Nulling length ratio		6
Slewing time	[s]	36 000
Time efficiency	[%]	80
Image size	[pixel]	256
Optimal wavelength	[μm]	15
Local zodi model	–	"darwinsim"
Habitable zone model	–	"MS"

Notes. See Dannert et al. (2022) for the definition and detailed description of the parameters. The first three parameters change in the different observing scenarios described in Table 2, the rest remain on DEFAULT value.

Table 2. Three observing scenarios for LIFEsim considered in this paper following Quanz et al. (2022b).

Parameter	OPTIMISTIC	BASELINE	PESSIMISTIC
Aperture (m)	3.5	2	1
Min. λ (μm)	3	4	6
Max. λ (μm)	20	18.5	17

Notes. "Aperture" describes the aperture diameter of the collector spacecraft.

planets. Quanz et al. (2022b) found that the wavelength range increases the yield of only a few percent, while an aperture diameter of $D = 3.5$ m resulted in an increase of around 100% (averaged over different scenarios) with respect to an aperture of 2 meters. It is important to mention that throughout the simulations the photon throughput was kept fixed at five percent (Quanz et al. 2022b). This is a rather pessimistic prediction to ground the simulations in but positive results can build confidence for the instrument's capabilities, especially with a higher photon throughput (Appendix B). We analyzed the impact of these instrumental parameters differences when observing higher temperature protoplanets. Within this paper, as a simplifying assumption, the planets are treated as blackbodies of different emission temperatures. Hot protoplanets will in fact show distinct emission features (Miller-Ricci et al. 2009; Lupu et al. 2014); however, the diversity expected for the variety of anticipated exoplanet compositions is large (Lichtenberg & Miguel 2024), and here we thus focused on scanning a larger parameter space with simplified assumptions. In Sect. 4.4 we discuss this decision and future plans to build on it.

When performing the simulations, we considered the different parameters stored in the data class of the simulator. Throughout the simulations we kept the planet's radius fixed at 1 Earth radius. For the planet's emission temperature, we considered high temperature cases where the atmosphere is transparent to

IR radiation, and moderate temperature cases where we assumed the emission temperature is affected by the greenhouse effect of the magma ocean atmosphere. For the high temperature cases, we considered temperatures of 1500 K, 2000 K, 2300 K, 3000 K, 4000 K, 7000 K and 10 000 K, which are in the range of typically molten surfaces (Lichtenberg et al. 2023). The upper limit of 10^4 K is an estimate for the emission temperature immediately after a giant impact event (Kegerreis et al. 2018, 2020; Lock et al. 2018, 2020). For moderate emission temperatures, we used values inspired by radiating temperatures from Lupu et al. (2014); Hamano et al. (2015); Lichtenberg et al. (2021); Boukrouche et al. (2021), with the effective temperatures of the planets ranging from 300 K to 800 K. All planet spectra used in the simulations are blackbodies.

2.2. Signal-to-noise ratio and detection

The output signal-to-noise ratio per wavelength bin, $(S/N)_\lambda$, is defined as the ratio between the photons detected from the exoplanet S_λ, and the expected number of photons coming from the noise sources N_λ (Dannert et al. 2022). We used Eq. (1) from Dannert et al. (2022) to obtain the total signal-to-noise ratio integrated over the entire considered wavelength range:

$$(S/N)_{tot} = \sqrt{\sum_\lambda \left(\frac{S}{N}\right)_\lambda^2}. \tag{1}$$

Following Dannert et al. (2022), we considered the detection threshold to be $(S/N)_{tot} \geq 7$, to compensate for the missing instrumental noise factor (Quanz et al. 2022b). We assumed that the instrumental noise contributes to the total noise less or equal to the astrophysical noise terms (see Eq. (3) in Sect. 4.4). The threshold of $(S/N)_{tot} = 7$ corresponds to a signal-to-noise ratio of astrophysical sources $(S/N)_{astro} \geq 5$. 2σ are added as an additional factor to account for the missing instrumental noise (see the discussion in Dannert et al. 2022). In future, a different threshold shall be used once the impact of instrumental noise in LIFEsim is accurately quantified. When the signal-to-noise ratio $(S/N)_{tot}$ of the simulation reaches seven we can consider the instrument capable of detecting the planet's signal. This is what we considered as detection within the context of this paper.

2.3. Nearby young stellar associations

Giant impacts that create magma ocean protoplanets typically take place in the early stage of a planetary system's lifetime. As a consequence of the decreasing number of planetesimals with time, the number of giant impacts around any star type decreases steeply with time, with most of them happening in the first 20 Myr after star formation (Quintana et al. 2016; Izidoro et al. 2021; Clement et al. 2022; Lichtenberg & Clement 2022). Because of the relation between stellar mass, number of giant impacts, and the size distribution of the resulting protoplanets (Bonati et al. 2019), the age and mass functions of the closest stellar associations are important factors when aiming to maximize the chances for detecting molten protoplanets (Bottrill et al. 2020). Therefore, while stellar associations containing a lot of M stars are more attractive when it comes to the likelihood of catching a planet in its magma ocean stage, these are typically smaller and hence less bright as their protoplanet counterparts around G and A stars, making them harder to detect (Bonati et al. 2019).

A list of known young stellar associations within 100 pc from the Solar System, taken from Bonati et al. (2019), can be found in Table 3. We used these as references when performing

Table 3. Young stellar associations with their respective distances to the geometric center of the group and age from Mamajek (2016).

Name	Distance (pc)	Age (Myr)
AB Doradus	20	150
β **Pictoris**	**37**	**23**
β Tucanae	43	45
Tucana Horologium	48	45
Columba	50	42
TW Hydrae	**53**	**10**
Carina	65	45
32 Orionis	92	22
η **Chamaeleontis**	**94**	**11**
χ 1 For	99	50

Notes. For β Pictoris' distance, the value found by Bonati et al. (2019) is used. Associations above the horizontal line are considered as Near, below the line as Far. The three associations studied in closer detail in this paper are highlighted in bold.

simulations and will examine a few of them further to evaluate the minimum integration times to detect cooling protoplanets around their stars. For the remainder of this paper, we will refer to the first seven associations (in order of increasing distance) as the Near group, while the remaining three (32 Orionis, η Chamaeleontis, and χ 1 For) as the Far group. This separation is due to a 30 pc gap between the two groups.

M-type stars

M-dwarf stars are of particular interest for detecting molten protoplanets because of their abundance relative to G-dwarf systems, among other considerations, such as their extended pre-main sequence phase. In Quanz et al. (2022b), simulations showed that the LIFE detection yield for planets around M-dwarfs was greater than for F, G and K stars due to their high occurrence rate in the Solar neighborhood. Observing young stellar associations that contain M-dwarf stars also directly increases the likelihood of detecting cooling protoplanets with LIFE. It is important to note, though, that the previous survey simulations were performed for systems no further than 20 pc away, so we assessed how the situation differs for systems at distances such as listed in Table 3.

Given the wide range of masses and temperatures the M star spectral class covers, for the simulations we used the well-studied M3 star AD Leonis. It has an effective temperature of 3390 K (Rojas-Ayala et al. 2012), a radius of 0.4 Solar radii, and a mass around 0.4 Solar masses (Reiners et al. 2009). For achieving the same equilibrium temperature as Earth, a rapidly rotating planet with zero bond albedo around AD Leonis would orbit at about 0.134 AU. We used this value to calculate orbits of interest for LIFE detection of terrestrial protoplanets. We remind the reader that we are interested in finding protoplanets with transient magma oceans, not atmosphere-stripped super-Earths or lava exoplanets, which are either permanently molten due to the intense irradiation (Piette et al. 2023) or have lost both primary and secondary atmosphere, exposing the planetary interior dynamics to extreme stellar forcing (Meier et al. 2021, 2023). Statistically, M-dwarf exoplanets are often found at these distances (Zhu & Dong 2021), hence no strong assumption is imposed.

Based on the above considerations, we picked three young stellar associations as the main reference cases. These are: β
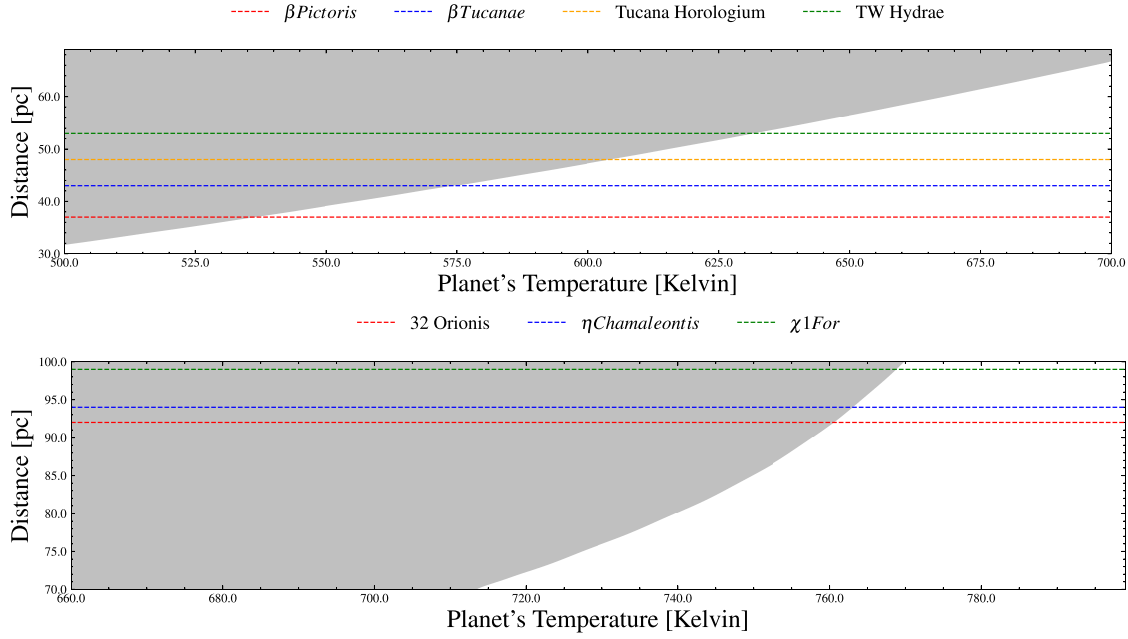
Fig. 1. Increase of maximum detectable distance with planetary emission temperature for an Earth-sized planet orbiting at 1 AU from a Sun-like star, after 10 hours of integration time. The gray area corresponds to a S/N value below seven (not detected) while the white is above seven (detected). Several prominent young stellar associations are plotted as horizontal lines at their respective distances. Top: near groups from Table 3. Bottom: far groups from Table 3.

Pictoris, TW Hydrae, and η Chamaeleontis. β Pictoris is considered a prime target for the detection of magma ocean exoplanets by Bonati et al. (2019). Although AB Doradus is the closest association, it may be too old to still contain magma ocean planets; thus β Pictoris is the closest association that will be considered in the simulations. It is also considered an observational target in Janson et al. (2023) because of its proximity and young age. The stellar association TW Hydrae is also of particular interest as it contains a lot of M stars among its population and is also particularly young, 10 Myr old. This, coupled with the fact that it is located at 53 pc away from Earth, makes TW Hydrae a very attractive candidate for detecting a cooling protoplanet in its magma ocean stage. Finally, η Chamaeleontis is the only stellar association from the Far group that we studied in greater detail. This again is due to its young age, far younger than the other two associations in the Far group (11 Myr as opposed to 22 and 50 Myr) and due to its high population of M stars. M-dwarf stars in far-away systems (e.g., η Chamaeleontis) can come close to the Inner Working Angle (IWA) of the instrument. See Sect. 4.4 for a discussion of this.

3. Results

3.1. Moderate temperature cases

Figure 1 shows how the detection capabilities change (white: detectable to above 7σ) as a function of emission temperature and distance, with several discussed young stellar associations indicated as dashed horizontal lines. The simulations are performed on an Earth-like planet orbiting a Sun-like star at 1 AU, with an integration time of 10 hours. Planets of temperature around 540 K are already detectable in the closest considered stellar association β Pictoris, while TW Hydrae's planets become detectable at around 635 K. As the temperatures reach a threshold around 750 K the increase becomes steeper as detection becomes relatively easier, due to the planet's thermal
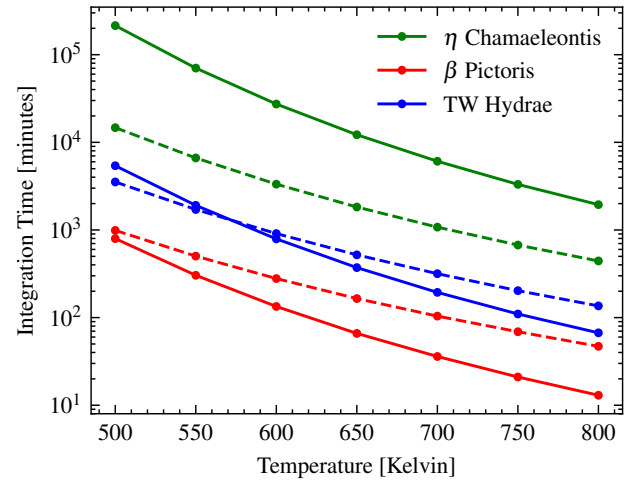

Fig. 2. Moderate temperature cases: minimum integration times necessary for detection against the planet's emission temperature. The dashed lines represent the results for a Solar-sized star host at 1 AU, while the solid lines are for M-dwarfs at 0.13 AU. The associations are at distances of 37 pc (β Pictoris, red), 53 pc (TW Hydrae, blue), and 94 pc (η Chamaeleontis, green).

emission becoming more significant. The farthest considered stellar association (χ 1 For) reaches detection at around 770 K. All considered associations within 100 pc become detectable below 800 K.

The results were reached with a fixed integration time of 10 hours. It is clear that integration time is a very important factor which can alter the results considerably, so it is important to perform simulations to study its effect at these temperatures for the relevant stellar associations, which we considered in Fig. 2. As the distance to the sun of the star-planet system increases in Fig. 2, the integration time required for detection also increases.
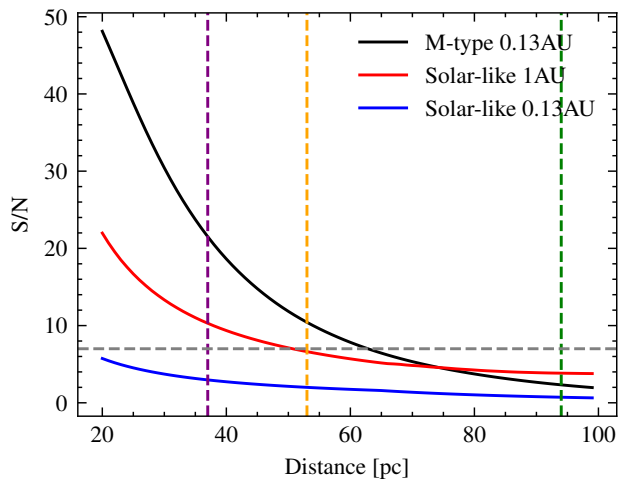
Fig. 3. Signal-to-noise ratio against distance for an Earth-sized 1500 K planet orbiting a Solar-sized and an M-dwarf star. All results are after 5 minutes of integration time and the vertical dashed lines indicate the distance to the associations β Pictoris (purple), TW Hydrae (orange), and η Chamaeleontis (green), respectively. The horizontal gray dashed line represents the considered detection threshold (S/N = 7).

Fig. 4. High temperature cases: minimum integration times necessary for detection against the planet's emission temperature. The dashed lines represent the results for a Solar-sized star at 1 AU, while the solid lines are for M-dwarfs at 0.13 AU. The associations are respectively at distances of 37 pc (β Pictoris, red), 53 pc (TW Hydrae, blue), and 94 pc (η Chamaeleontis, green).

The distances are 37 pc (red), 53 pc (blue), and 94 pc (green) and in all three cases the trends of the curve are almost identical. The integration time decreases exponentially as the temperature of the observed planet increases.

For M-dwarf-orbiting planets, the necessary integration times are consistently shorter for β Pictoris. For TW Hydrae they are shorter for temperatures above 600 K, while for Chamaeleontis they are consistently much higher than their G star counterparts. Targets are easier to detect around M stars at shorter distances but harder to detect at larger distances (with respect to targets orbiting G stars) because the targets orbiting M-dwarf stars at 0.13 AU fall within the IWA of LIFE in the farther association η Chamaeleontis. At shorter distances, for β Pictoris, the times at 500 K are respectively almost 1000 minutes (16.6 h) for the Sun-like star and 800 minutes (13.3 h) for the M-dwarf. Yet at 800 K the times are much closer to each other, only 40 minutes apart.

3.2. High temperature cases

For protoplanet cases where the emission temperature is 1500 K or higher the situation is quite different (Fig. 3). The maximum detectable range in this case extends much farther. While the plot only shows results for distances up to 100 pc, these were obtained with a very short integration time of 5 minutes. The instrument can therefore reach detection at greater distances if enough time is employed.

At integration times of 10 hours, the results of Fig. 1 indicate that the relation between distance and the planet's temperature is not linear. The distance reached after 10 hours at a temperature of 1500 K is more than double compared to the distance at 750 K. Furthermore, Fig. 1 shows that for reasonable integration times, LIFEsim is able to detect a protoplanet in its magma ocean stage in the galactic neighborhood (<100 pc) where the considered stellar associations reside.

The S/N values from Fig. 3 decrease with distance as farther objects are more difficult to observe. It is important to note that, for LIFEsim, it is easier to observe planets orbiting M-dwarfs at 0.13 AU than the same planet orbiting a Solar-sized star at 1 AU,
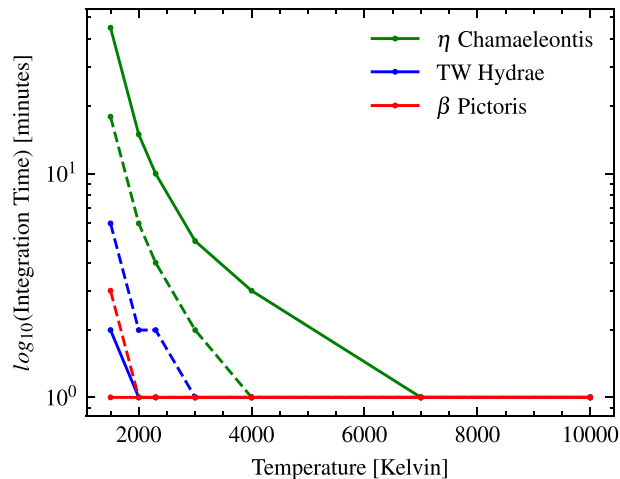
albeit for shorter distances, roughly up to 70 pc. Although the S/N values do converge at greater distances. With 5 minutes of integration time if the planet orbits a Solar-sized star at 0.13 AU, LIFE would not be able to detect it even in β Pictoris as the stellar leakage would make it impossible to observe (Fig. 3).

3.2.1. G and M-dwarf star comparison

Figure 4 represents the minimum integration times necessary for detection of an Earth-sized planet for the high temperature cases. For the two closer associations, protoplanet detection for the M-dwarf cases at the respective orbits would theoretically only require one or two minutes of integration time. For η Chamaeleontis, the situation is very different with 45 minutes of integration time needed for the fainter planet. Results reach the 1 minute limit at around 7000 K. For the orbit around a Solar-sized star the situation is different, with slightly higher times necessary (for β Pictoris and TW Hydrae) at lower temperature but still only a few minutes are required. The lowest temperature planet reaches a maximum of 18 minutes in the farthest association η Chamaeleontis.

3.2.2. Varying LIFE parameters: Solar-sized stars

So far, all the results presented were simulated in the BASE-LINE scenario of LIFEsim. Next, we studied the other observing scenarios and evaluated their performance and limitations. Fig. 5 demonstrates a substantial difference between the different observing scenarios, for simulations on Sun-like stars. In the OPTIMISTIC scenario planets with temperatures of 2000 K or more only need 1 minute of integration time to be detected in all three stellar associations. In the BASELINE scenario, the three associations "flatline" at 1 minute, each at different temperatures, respectively at 2000, 3000 and 4000 K. The PESSIMISTIC scenario, as expected, is the one that requires the most integration time, with the closest association β Pictoris reaching 1 minute at 7000 K. The better performance of the optimistic scenario is due to its wider aperture diameter and wavelength range which allows for more signal to be collected from the targets.
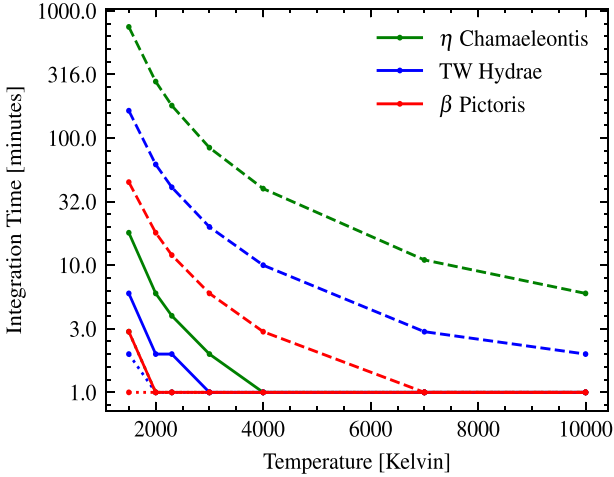
Fig. 5. Varying LIFE parameters – G star: minimum integration times necessary for detection against the planet's emission temperature for an Earth-sized planet orbiting a Solar-sized star at 1 AU. The simulations were performed in the PESSIMISTIC (dashed), BASELINE (solid), and OPTIMISTIC (dotted) scenarios. The associations are respectively at distances of 37 pc (β Pictoris, red), 53 pc (TW Hydrae, blue), and 94 pc (η Chamaeleontis, green).
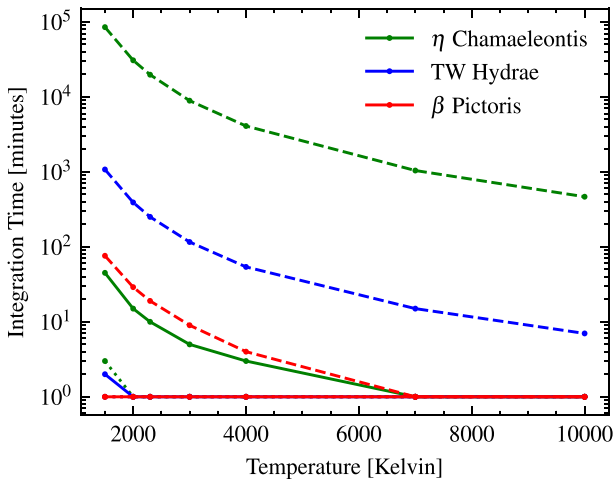

Fig. 6. Varying LIFE parameters – M-dwarf: minimum integration times necessary for detection against the planet's emission temperature for an Earth-sized planet orbiting an M-dwarf at 0.13 AU. The simulations were performed in the PESSIMISTIC (dashed), BASELINE (solid), and OPTIMISTIC (dotted) scenarios. In the optimistic scenario, all times are 1 minute. The associations are respectively at distances of 37 pc (β Pictoris, red), 53 pc (TW Hydrae, blue), and 94 pc (η Chamaeleontis, green).

The reason 1 minute is the minimum integration time is that we manually set it to that value. While the simulator allows for simulations down to one second, in a real setting, the instrument will not perform observations of such short times. In Figs. 5 and 6, the lines that are not visible overlap at the 1 minute level as they are all flat.

3.2.3. Varying LIFE parameters: M-dwarf stars

We performed the same simulations, as in the previous section, for M-dwarfs. The results are displayed in Fig. 6. In the PESSIMISTIC scenario, β Pictoris requires slightly more than an hour for the fainter planet (76 minutes), TW Hydrae requires
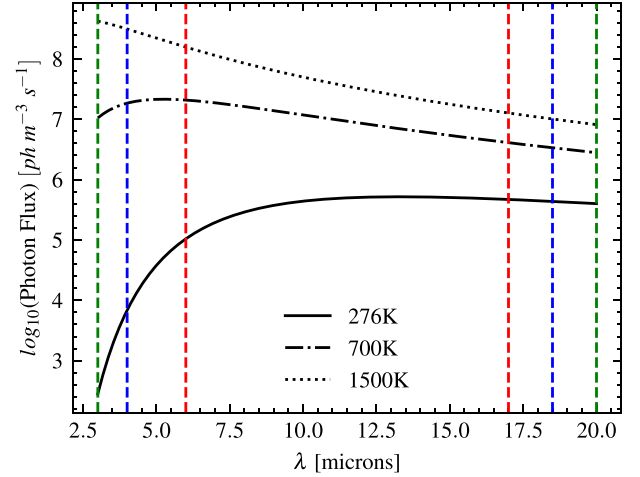
Fig. 7. Photon flux emitted by a blackbody against the wavelength (microns). Blackbody curves of three planets at 276, 700, and 1500 K respectively. The vertical lines represent the wavelength ranges considered for the PESSIMISTIC (red), BASELINE (blue), and OPTIMISTIC (green) LIFE scenarios.

almost 18 hours while Chamaeleontis requires 1416 hours. In the BASELINE scenario plot β Pictoris is always 1 minute and TW Hydrae from 2000 K onward, while η Chamaeleontis reaches it at 7000 K. In the OPTIMISTIC scenario all three associations require 1 minute of integration time throughout the whole temperature range. Notably, the integration time is below one hour in all cases.

3.3. Influence of wavelength range on received total flux

As one can see in Table 2, the observing scenarios differ in two ways, the wavelength range considered and the aperture diameter of the collector spacecrafts. Quanz et al. (2022b) found that the aperture diameter greatly affected the detection rate in their simulations, more significantly than the wavelength range. In the plots showcasing the integration times for the different scenarios (Figs. 5 and 6) it is clear that, while the BASELINE and OPTIMISTIC scenarios are relatively similar to each other, the PESSIMISTIC scenario differs a lot from the other two. The BASELINE and PESSIMISTIC scenarios differ both in wavelength range and aperture diameter, with the aperture being 50% of the BASELINE scenario. On top of this, the BASELINE and OPTIMISTIC scenarios have different aperture diameters yet very similar results.

The reason for this disparity in the results also lies in the temperature of the observed planets. While Quanz et al. (2022b) treated low temperature planets around the same effective temperature as the Earth, in this paper we dealt with planets up to 10 000 K. At higher temperatures, the emission starts to become increasingly dominated by shortwave radiation. This can be seen clearly in Fig. 7. For a 276 K planet, the flux ratio integrated over all wavelengths between the PESSIMISTIC and BASELINE scenario is 88%, while it is 82% for PESSIMISTIC over OPTIMISTIC. On the other hand, for a 1500 K planet, the PESSIMISTIC over BASELINE ratio is of 40% and PESSIMISTIC over OPTIMISTIC is at 24%. This means that the PESSIMISTIC scenario receives only 40% of the photon flux from a 1500 K planet compared to the BASELINE scenario, and 24% of the OPTIMISTIC one.

These results indicate that for the hotter planets we considered, the shorter wavelength regions become more important
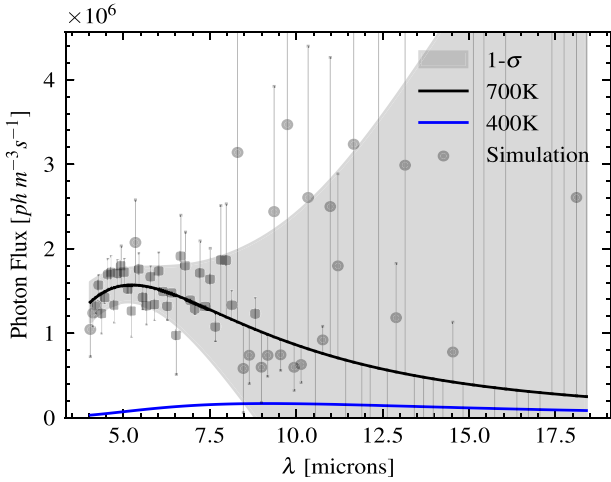
Fig. 8. Photon flux against wavelength comparing planets at 700 K (black) and 400 K (blue) emission temperature, respectively, with the BASELINE scenario parameters. The gray area represents the statistical difference of 1σ from the 700 K planet. The scattered points are random noise to simulate the received flux from the warmer planet.
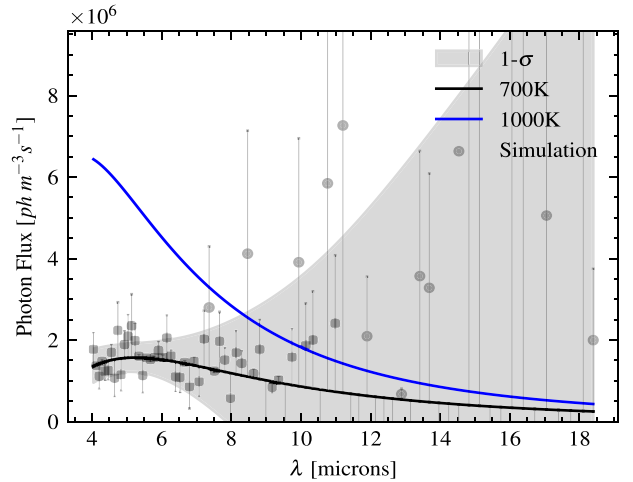

Fig. 9. Photon flux against wavelength comparing planets at 700 K (black) and 1000 K (blue) emission temperature, respectively, with the BASELINE scenario parameters. The gray area represents the statistical difference of 1σ from the 700 K planet. The scattered points are random noise to simulate the received flux from the cooler planet.

as they contain more photon flux from the observed planet. Boukrouche et al. (2021) similarly found a shift in the spectrum toward shorter wavelengths (i.e., the visible regime) for correlated-k radiation transport simulations of steam-dominated atmospheres at runaway greenhouse conditions, which corroborates our findings despite the simplified blackbody assumptions.

3.4. Constraining radiating temperature

In order to study how well LIFE could constrain a planet's temperature, we performed simulations on two planets with different temperatures and evaluated the resulting statistical difference. The simulations were performed for Earth-sized planets orbiting an M-dwarf star at 0.13 AU. The distance to the system is 37 pc, as β Pictoris. The cases studied in this paper are that of a 400 K and a 1000 K planet, each compared to a planet emitting at 700 K. The reason to simulate these cases is that the realistic emission temperature of a magma ocean planet would depend sensitively on its composition (redox state) and total volatile inventory; hence we tested variations of several hundred Kelvin against each other. The uncertainty per bin was computed following

$$\sigma_{bin} = \frac{F_{planet,bin}}{(S/N)_{bin}}, \qquad (2)$$

where $F_{planet,bin}$ is the blackbody flux of the planet per wavelength bin and $(S/N)_{bin}$ is the signal-to-noise ratio per bin obtained by the instrument after the observation. The gray area in Figs. 8 and 9 represents the 1σ statistical distance and the scattered points represent the blackbody flux with a random noise (between 0 and σ_{bin}) to simulate the received flux. The uncertainty is calculated for the standard 700 K planet, and the two plots represent the results when a +300 and −300 K planet's blackbody are plotted against this. For these simulations, the spectral resolution of the instrument was set to 50.

Figures 8 and 9 demonstrate further that the shorter wavelength regions become increasingly important for hotter emission temperatures. Below ∼10 μm, the noise is low but increases at longer wavelengths. Figure 10 shows that the statistical difference between the planets in both cases is above the 5σ level
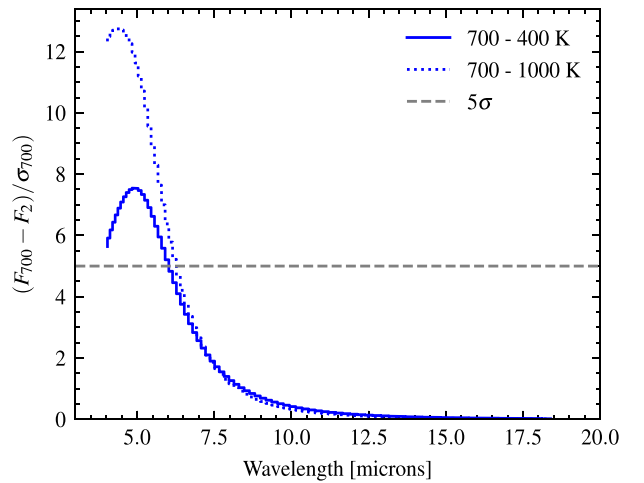
Fig. 10. Flux difference in units of σ against wavelength for the two case studies of a 400 K or 1000 K compared against a 700 K protoplanet. F2 refers to the flux F_{700} is compared against. The horizontal line marks the 5σ threshold.

only below $\lambda = 6$ μm. This means the LIFE mission would only be able to discriminate the emission temperatures in the significant climate regime for runaway greenhouse planets in this range for the BASELINE scenario (the OPTIMISTIC would offer a wider range). While the results of the analysis are shown per wavelength bin, the whole spectrum will be employed to determine the target planet's temperature. Therefore, regardless of the worse distinguishing power of longer wavelengths at these temperatures, an overall stronger distinction than 5σ between the two models will be reached. In Fig. 10 it is clear that while the two cases have the same temperature difference in magnitude (300 K), the result is more promising for the hotter planet case as more signal is collected and the uncertainty per bin decreases. The 700–1000 curve reaches a peak of almost 13 σ while 700–400 reaches close to 8 σ.

Figure 11 shows how the peak sigma value of the statistical difference between the planets varies with temperature difference and observation time. As expected, the greater the
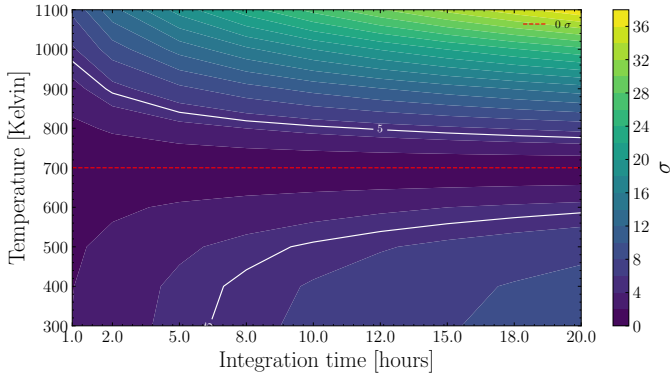
Fig. 11. Contour plot of the peak sigma value, from the statistical difference curve, for protoplanets of different emission temperatures against a 700 K planet.

temperature difference and integration time, the higher the sigma value. The statistical difference increases faster for higher temperatures as the magnitude of the flux affects the observations, making it easier to distinguish fluxes for LIFEsim.

3.5. Exozodi dust study

An additional factor that plays an important role in observations of young stellar systems is exozodiacal dust. It is expected that dust in young systems only tens of Myr old can reach very high levels compared to the Solar System (Defrère et al. 2010; Vican & Schneider 2014; Kral et al. 2017; Absil et al. 2021). For this reason, we performed simulations in the BASELINE scenario to study how exozodiacal dust affects LIFE's performance. Within these simulations, we employed the exozodi dust prescription as introduced in Dannert et al. (2022); hence we limited the exploration to dust belts similar to the terrestrial planet zone of the Solar System. To keep the main body of the paper at a reasonable length, we discussed only four scenarios as per Fig. 12. A more extended parameter study can be can be found in Appendix A.

The contour plots in Fig. 12 show that for the high temperature cases, levels of 1000s of zodis do not pose a problem for detection. The parameter "z" is a measure of the zodis of a system, it is a unit that indicates the level of exozodiacal dust. One zodi (z=1) corresponds to the Solar System level of zodiacal dust, z=2 is double and so on. It is therefore a global scaling factor. The planet orbiting an M-dwarf obtains higher values for S/N consistently than its G-star counterpart, for example in the (d) plot the $S/N = 10$ line is outside the bounds of the plot. The results obtained for the 1500K planet indicate that even in the farthest association, with exozodiacal dust at levels thousands of zodis, LIFE is capable of detecting protoplanets. Realistically it will require times longer than the few minutes obtained in previous sections for z=3 but still reasonable times. For a more detailed study see Appendix A.

For the moderate temperature case of 700 K the situation is different. The detection limit for a Sun-like orbiting planet at 1AU drops drastically, with detection becoming impossible for a thousand zodis even at 20 pc. See Appendix A for a comparison with results after longer integration times. For M-dwarf-orbiting planets detection is still possible up to almost 70 pc for z=10^3, meaning that with a reasonably longer integration time, detection at the farthest association can be reached.
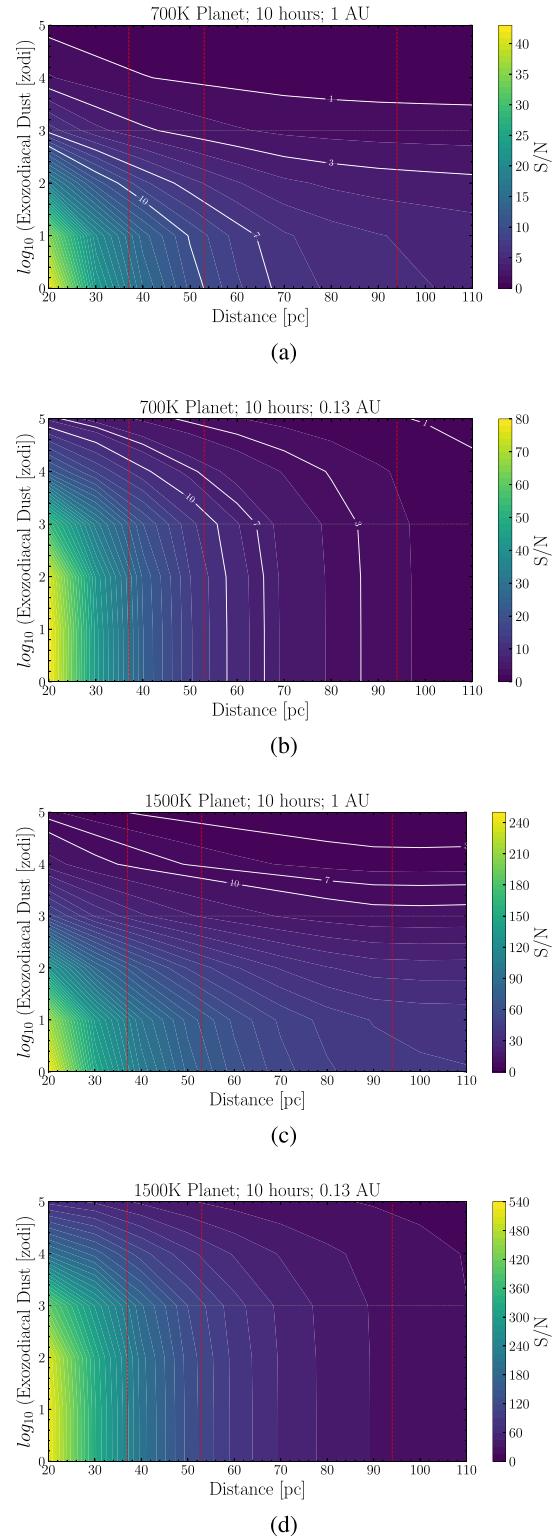

(a)

(b)

(c)

(d)

Fig. 12. Resulting S/N obtained after observation of a planet in a system with different exozodi dust levels. All four plots are obtained with 10 hours of integration time and for observation of a planet in the farthest stellar association η Chamaeleontis. Plots (a) and (b) are observations for a moderate temperature case, 700 K, (c) and (d) are for a 1500 K scenario. For each temperature case, the first plot is for a planet orbiting a Sun-like star at 1 AU, the second is for an M-dwarf at 0.13 AU. The red vertical lines indicate the distances of β Pictoris, TW Hydrae, and η Chamaeleontis, respectively.
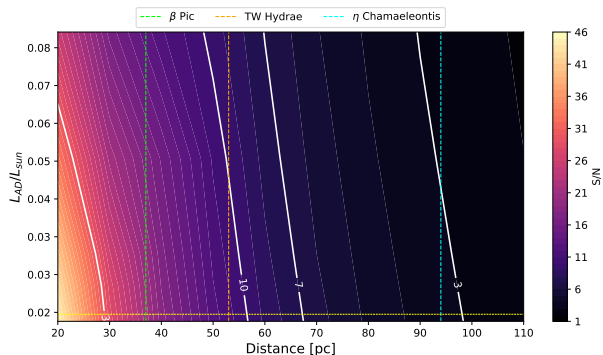
Fig. 13. Countour plot of the S/N for a 1500 K planet orbiting AD Leonis M-dwarf star (orbit of 0.13 AU) at different luminosity (*y*-axis) and distance (*x*-axis), after one hour of integration time. The horizontal yellow line indicates the current AD Leonis to Sun luminosity ratio.

3.6. M star varying luminosity

In the early stages of their lifetime, M-dwarf stars are orders of magnitude brighter than their main sequence luminosity (Baraffe et al. 2015). This paper focuses on M-dwarf stars in young stellar associations of the order of tens of Myr. Therefore it is important to explore how the luminosity of a star such as AD Leonis affects simulations at different stages of its early life (see Fig. 13). The y-axis of Fig. 13 represents the ratio of the luminosity of AD Leonis and the Sun's luminosity, corresponding to different periods of the star's lifetime. The maximum of the luminosity corresponds to 10 Myr after star formation and the minimum at the current age luminosity (Baraffe et al. 2015). The x-axis is the distance to the system. In the earlier stages of its lifetime (high y-value) AD Leonis would be brighter than it is currently; therefore the ratio is higher. As time passes it decreases in luminosity until it reaches the horizontal yellow line which is the current AD Leonis luminosity to Sun's luminosity ratio.

Figure 13 shows that tracing back to the earliest stages of AD Leonis' lifetime the resulting detection distance varies by 5–6 pc at most. At its youngest stage, the simulation's detection capability reaches around 62–63 pc, hile at the current stage, it is at 67–68 pc at most. These results suggest that the fact that M-dwarf stars are brighter in the early stages of their lifetime will not significantly affect the observations of LIFE. Our results corroborate this for a 0.4 $M_\odot$ M-dwarf. For moderate temperature cases, detection can still be reached at similar distances with reasonable integration times.

4. Discussion

4.1. Distance range and integration times

A major conclusion from our analysis is that the detection range for hot protoplanets of the LIFE concept extends in principle to a hundred parsecs, considerably beyond the local Solar neighborhood. While the currently considered nominal ranges for potentially habitable planets for the LIFE survey are limited to nearby stars within 20 pc, the results obtained here provide strong support for considering observations further out in young stellar systems. Magma ocean atmospheres with emission temperatures in an intermediate range of a few hundred K are detectable after a reasonable integration time of 10 hours up to 100 pc and beyond. These results indicate that planets in the considered stellar associations can be detected with shorter integration times. In addition, a very high S/N for these

planets can easily be obtained to characterize the magma ocean atmosphere in greater detail.

The main goals of this paper were to study LIFE's interferometer ranges and limits, considering different instrumental scenarios when it comes to observing a magma ocean protoplanet. At present, the study of such hot atmospheres is focused on analyses of steam-dominated runaway greenhouse climates (e.g., Goldblatt et al. 2013; Leconte et al. 2013; Goldblatt 2015; Leconte et al. 2015; Pluriel et al. 2019; Graham et al. 2021; Boukrouche et al. 2021; Chaverot et al. 2022; Turbet et al. 2021). During the early cooling phase after formation, these planets have brightness temperatures beyond 2000–3000 K, with high temperature situations reaching up to 10 000 K immediately after collision events. Importantly, planets in steam-dominated runaway greenhouse climate states will likely settle into an equilibrium point dictated by transmission through the two main water opacity windows (Goldblatt et al. 2013; Boukrouche et al. 2021). The equilibrium point in a runaway greenhouse climate is highly sensitive to the total water column and cloud distribution, and hence total atmospheric pressure, which makes observations of different planets in the runaway regime highly desirable for studying the deviation of volatile contents across planetary systems and the early climatic evolution of terrestrial protoplanets (Wordsworth & Kreidberg 2022; Schlecker et al. 2024). In this paper, we used LIFEsim to study the minimum integration times necessary to detect such scenarios with LIFE, with a focus on the young stellar associations β Pictoris, TW Hydrae, and η Chamaeleontis. These associations are young (in the range of a few Myr) as it makes it more likely to find young stars with magma ocean planets in their stars' orbit (Bonati et al. 2019).

There is a clear difference between observing Solar-sized and M-dwarf stars, but for both cases the BASELINE and OPTIMISTIC scenario stay below one hour integration time for the faintest considered protoplanet, among the high temperature cases, in the farthest stellar association. These results suggest that, with reasonable amounts of observing time spent on these stellar associations, there is a good chance of detecting a magma ocean protoplanet. Collecting more signal from a single planet is then comparably cheap in follow up studies, as a higher S/N can give more information on the object. Furthermore, the instrument's performance in the different observing scenarios showed interesting results. While Quanz et al. (2022b) found that the aperture diameter affected the detection yield considerably more than the wavelength range (as for more temperate planets), the results obtained in this paper partly differ from this. It is worth pointing out that they considered a much wider sample in terms of both mass and age, focusing on mature exoplanets. The PESSIMISTIC scenario, which differs from the BASELINE scenario in both aperture diameter and wavelength range, displays much higher integration times. The OPTIMISTIC and BASELINE have a 1.5 m difference in aperture yet very similar results. The reason why the PESSIMISTIC scenario with its 1-m aperture diameter is so different can also, at least partly, be attributed to diminished wavelength range. These results indicate that restricting the wavelength range in the shortwave greatly affects the integration time necessary for the detection of molten protoplanets. The reason for this lies in the shift of the spectrum of hotter planets toward shorter wavelength ranges, compared to more temperate climate regimes.

Finally, it is important to mention that with regard to integration time, observational planning will need to consider the slewing time. In the LIFEsim environment, this time is set at 10 hours by default and it indicates the amount of time required to point the telescope toward a new target. This value will

become more accurate in the future and varies depending on which targets it is moving between. The extremely short integration times per target star for reaching the detection threshold opens up the possibility of scanning essentially all young stars within the most ideal associations for the presence of terrestrial protoplanets. Magma ocean lifetimes of oxidized planets beyond the runaway greenhouse threshold are thought to last ~Myr (Salvador et al. 2017; Salvador & Samuel 2023; Hamano et al. 2015; Luger & Barnes 2015), with potentially prolonging effects of primordial H-rich envelopes (Lichtenberg et al. 2021). The probability distribution of giant impacts beyond ~10 Myr after stellar formation is strongly sensitive to the number of remaining planetary embryos at this stage (Clement et al. 2020, 2022).

4.2. G vs. M-dwarfs

As outlined in Quanz et al. (2022b), LIFE shows a considerable positive bias toward finding exoplanets around M-dwarf stars, at least up to around 70 pc. Here, we further explored this effect by directly comparing the performances of Solar-sized against M-dwarf stars. In this paper, we considered orbital distances of 0.13 AU for M-dwarfs. As a consequence of this, the smaller angular separation negatively affects simulations. M-dwarfs consistently require longer integration times for η Chamaeleontis (94 pc) and for 500 and 550 K planets (Fig. 2) at TW Hydrae (53 pc). For the rest of the simulations, they perform better (or the same when overlapping at 1 minute) than their G star counterpart. Furthermore the S/N trends in Fig. 3 suggest that while it is better to observe planets around M-dwarf stars at shorter distances, the situation gets inverted after a certain point. As one can see in Fig. 3 the curves intersect at approximately 75 pc. Beyond that, the S/N obtained from the planet orbiting a Solar-sized star becomes greater. The reason for this intersection is likely related to the angular separation of the planet at those distances being very small and therefore requiring greater integration times. However, observing around M-dwarf stars fundamentally carries angular resolution as an instrumental limitation. As previously discussed, when observing around M-dwarfs one needs to consider smaller orbits as those are the distances at which planets tend to form and orbit around these stars (Zhu & Dong 2021). See the extended discussion on angular separation limitations for M-dwarf planetary systems in Sect. 4.4.

Planets around M-dwarfs are anticipated to be locked in continuous runaway greenhouse phases for the first few hundred Myr of their lives because of the superluminous pre-main sequence phase of small stars (Ramirez & Kaltenegger 2014; Luger & Barnes 2015; Wordsworth & Kreidberg 2022; Lichtenberg & Clement 2022). This would give ample opportunity to observe magma ocean atmospheres in these planetary systems. The demographic trend of this extended runaway greenhouse phase should be observable already by transit missions (Turbet et al. 2019), especially PLATO (Schlecker et al. 2024). If detected statistically, LIFE will have substantial opportunity to study magma ocean atmospheres and climatic diversity if pointed toward a young M star planetary system. These investigations will also allow for a better understanding of the ability of M-dwarf orbiting planets to retain their atmospheres.

Our work in this paper purely focuses on the simulated performance of the LIFE instrument in the detection and retrieval of hot protoplanets. The likelihood of detecting such objects in stellar systems is an important factor to take into account when considering a viable survey strategy. An initial study of the occurrence rates and timescales of hot protoplanets in young stellar systems has been performed in Bonati et al. (2019). In said paper, they modeled the frequency of giant impact collisions using classical N-body planet formation models and the cooling of the resulting magma oceans, to calculate the likelihood of detecting "at least one magma ocean planet" in different stellar associations. They found that young stellar systems such as β Pictoris and TW Hydrae are promising candidates for molten protoplanets detection with young stellar systems having higher occurrence rates of post-impact planetary objects. Our simulations here indicate shorter integration times necessary for detection, meaning that less observation time can be allocated to a single planet than was discussed in Bonati et al. (2019). It is important to emphasize the actual number of giant impact events in young planetary systems across the stellar mass spectrum is subject to considerable uncertainty, in particular across the range of end-member planet formation scenarios from pebble- (e.g., Morbidelli & Nesvorny 2012; Lambrechts et al. 2019; Johansen et al. 2021, 2023; Olson et al. 2022; Olson & Sharp 2023) to planetesimal-based (e.g., Alibert et al. 2013; Quintana et al. 2016; Wyatt et al. 2019; Emsenhuber et al. 2021; Schlecker et al. 2021a,b; Clement et al. 2020, 2022; Lichtenberg & Clement 2022) accretion frameworks. Therefore, the detection of molten protoplanets in such systems will serve to critically constrain the planetary accretion scenarios. A dedicated study to assess the survey trade-offs regarding slewing time between individual observations of young planetary systems and the predictions from end-member planet formation models should be conducted in future work.

Throughout this paper, we used a maximum nulling baseline of 100 meters similar to previous LIFE publications, which might be subject to change in the future. If one considers longer baselines, such as the maximum baseline of 168 meters assumed by Bonati et al. (2019), observations become easier around M-dwarfs at 0.13 AU for β Pictoris, TW Hydrae and η Chamaeleontis. An increased nulling baseline would therefore increase the opportunity to detect and characterize protoplanets around M-dwarfs in these stellar associations. See Sect. 4.4 for an extended discussion.

4.3. Sensitivity to wavelength range

We found that observing scenarios with a restricted wavelength range and aperture (e.g., the PESSIMISTIC scenario) perform worse than the other scenarios. Figure 7 and the noise distribution in Figs. 8 and 9 suggest the shorter wavelengths regime rather than longer wavelengths as the reason for this discrepancy. By restricting the shorter wavelengths, the PESSIMISTIC scenario collects much less photon flux from the target planet. In the 1500 K case for example, we found that 24% of the flux the OPTIMISTIC scenario collects can also be collected by the PESSIMISTIC scenario, most of the missing flux lying in the short wavelengths (by several orders of magnitude). Furthermore, LIFE can distinguish between different emission temperatures better at lower wavelengths with σ_{bin} becoming larger with increasing wavelength. For the purpose of constraining the effective temperature of a planet, wavelength regions < 6 µm are more important than > 17 µm.

4.4. Limitations

The results discussed in this paper are simulated, necessarily restricting the realism of the obtained noise estimations. The LIFE simulator includes all major astrophysical noise terms (e.g., zodiacal and exozodiacal dust, stellar leakage), which are

always included in the simulations and accounted for in the final results. Quanz et al. (2022b) and Dannert et al. (2022) studied the noise terms and their contributions in depth. They found that stellar leakage noise dominates in the short wavelength range, while at longer wavelengths the zodiacal dust becomes the main noise source. This is due to the fact that in the Solar System the zodiacal dust is an important source of MIR emission, well in the wavelength range of the LIFE interferometer (Quanz et al. 2022b).

The LIFE simulator currently only includes the treatment of exozodiacal dust (see Appendix A) for the photon noise from habitable zone dust. It does not yet include a treatment of potential dust structures in the terrestrial planet region, that could cause confusion and hence mimic or hide the signal from a planet, neither does it include potential signals from hot dust closer to the star which is observed around a fraction of stars (Defrère et al. 2010; Vican & Schneider 2014; Kral et al. 2017; Absil et al. 2021). It will thus be important to incorporate a more elaborate treatment of exozodis to probe the potential for observing these systems with LIFE.

Furthermore, detector related noise and thermal background from the aperture mirrors and/or instrument optics are not included in the simulations yet. This is partly due to the fact that the instrument does not physically exist and the initiative is still considering different detectors and combiner architectures (Dannert et al. 2022; Hansen & Ireland 2022; Hansen et al. 2023). In this paper we dealt with this problem as in Quanz et al. (2022b), assuming that the instrumental noise contributes to the total noise less or equal to the astrophysical noise terms and that the total noise can be calculated using:

$$\sigma_{tot} = \sqrt{(\sigma_{inst})^2 + (\sigma_{astro})^2}, \tag{3}$$

where σ_{inst} and σ_{astro} are the instrumental and astrophysical noise terms respectively. By then choosing a S/N ≥ 7, corresponding to a S/$N_{astro} \geq 5$, as the detection threshold, we hope to compensate for the lack of the instrumental noise term. A noise model is currently under implementation in LIFEsim. As of now, LIFEsim assumes that the shot noise (e.g., stellar leakage) will dominate over the instrumental noise (Dannert et al. 2022). Our results highlight the importance of shorter wavelength regimes for the LIFE mission, thus we need better modeling in these regimes where instrumental noise may dominate.

Especially for the more distant systems in our study, the inner region of the habitable zone tends to present at very small angular separations from the host star (e.g., the inner edge of the habitable zone around a $0.4\,M_\odot$ star in η Chamaeleontis is at 1.2 mas). With the nulling baseline limited to 100 m this leads to these regions being well inside the typical Inner Working Angle (IWA), which is defined as the angular separation where the interferometric transmission drops to below 50% (IWA$_{10\,\mu m}$ = 5.2 mas). For these targets, LIFEsim correctly accounts for the low transmission. Close-in targets remain nonetheless detectable in photon count statistics because of their large midinfrared luminosity $L_{bol} \sim T^4$ induced by their high effective temperatures. However, for distinguishing between the planetary and stellar signal, signal extraction in nulling interferometry relies on the modulation of the planetary signal by movement of the collector array (see Dannert et al. 2022). In the assumed setup, the signals of planets well within the IWA receive a relatively low number of modulations per array rotation, which in turn can complicate signal extraction, especially in the presence of low frequency instability noise (Lay 2004, 2006). This can be mitigated by allowing for longer nulling baselines. We plan to

explicitly address this in future work by running detailed signal extraction on distant forming terrestrial exoplanets.

From a target perspective, all our simulations use idealized blackbodies to simulate protoplanets of different emission temperatures. This is a substantial simplification, as atmospheres of varying compositions and emission temperatures differ greatly in their spectra. However, at high temperatures and pressures in the regime studied here, current climate simulations predict the emission to start behaving as a blackbody again (Boukrouche et al. 2021; Lichtenberg et al. 2021; Chaverot et al. 2022; Selsis et al. 2023). This is, to some extent, rooted in the missing laboratory data on high temperature opacities (Fortney et al. 2019). Given the current uncertainties regarding high temperature and high pressure atmospheres over a wide composition array, our approach yields initial insights into the potential for observation. This limitation also touches on the principal degeneracy in Sect. 3.4 between planetary emission temperature and surface. Typically, both are particularly degenerate with each other at short wavelengths. However, in the midinfrared this degeneracy can be broken because deeper regions of the atmosphere can be accessed (e.g., Wordsworth & Kreidberg 2022; Konrad et al. 2023). Therefore, we plan to significantly extend the current study, which focused on the detection of hot protoplanets, by simulating magma ocean atmospheres with more realistic climate models (e.g., Wordsworth et al. 2018; Janssen et al. 2023), to capture their anticipated diversity (Suer et al. 2023; Lichtenberg & Miguel 2024; Kempton et al. 2023; Kempton & Knutson 2024) and assess the level of detail that can be retrieved.

5. Conclusions

In this paper, we investigated the range and required integration times for the detection of hot terrestrial protoplanets with the LIFE mission concept. We considered different parameters for the potential protoplanets and host stars, focusing on the planet's and star's temperature and radii. Additionally, we studied the detection capabilities of LIFE for protoplanets around M-dwarfs and evaluated the performance of different instrumental scenarios of LIFE and their potential for discriminating the emission temperature of a given protoplanet. Our main findings can be summarized as follows:

– The detection range for finding terrestrial protoplanets with LIFE extends far beyond the direct Solar neighborhood, potentially reaching distances up to a hundred pc. A number of potentially interesting young stellar associations sit at distances ranging from 20 up to 95 pc. The Large Interferometer For Exoplanets can detect an Earth-sized magma ocean planet with integration times of minutes to hours at these distances;

– Detecting protoplanets with LIFE is generally easier for M-dwarf host stars. The simulations mostly showed better results (higher S/N and lower integration times) within this spectral type domain at distances below ∼70 pc, compared to G stars.

– The angular resolution of the instrument negatively affects the detectable orbital distance of terrestrial protoplanets past the direct Solar neighborhood for M star targets. However, the anticipated performances of all considered LIFE scenarios still allow for detection within the terrestrial planet forming zone, in particular during the pre-luminous main sequence phase of M-dwarfs, which increases the likelihood of runaway greenhouse phases and thus magma ocean atmospheres;

– The performance of different instrumental design choices was evaluated and we found the PESSIMISTIC scenario to be more distinct from the other two analyzed scenarios. Our results indicate that the wavelength range being restricted in the shortwave affects the instrument's performance just as much, if not even more, than the aperture diameter. The shorter wavelength range is important when observing hotter planets because of the increase in shortwave emission at these temperatures;

– Because of this, discriminating the emission temperature of hot protoplanets with LIFE works better at shorter wavelengths. The resulting statistical difference between the observed planets passed the 5σ detection threshold only at <6 μm. Nonetheless, when integrating over the whole spectrum, the resulting distinction will be greater than 5σ;

– The main limitations of our study are related to (i) the expected non-blackbody nature of protoplanet atmospheres, (ii) the limits to the inner working angle of LIFE for far-away systems, and (iii) the lack of an instrumental noise model. These limitations will be addressed in future work.

In summary, the LIFE mission concept is capable of detecting and characterizing bright cooling protoplanets up to 100 pc. While these distances are not considered in the main target range for LIFE's core tasks, our results encourage observing targets in distinct young stellar associations at far greater distances from the Solar System. Typically, LIFE requires integration times of only minutes to a few hours for initial detection of protoplanet candidates. Characterizing terrestrial protoplanets would greatly contribute to our understanding of atmospheric formation on terrestrial planets, and provide detailed insight into the physical and chemical processes that occur during the transition from primary to secondary atmospheres, elucidating the conditions available for prebiotic chemistry on young worlds.

Data availability

The computer code to reproduce the results of this paper is openly available at https://github.com/FormingWorlds/LIFE_MagmaOceanDetection.

References

Absil, O., Marion, L., Ertel, S., et al. 2021, A&A, 651, A45
Alei, E., Konrad, B. S., Angerhausen, D., et al. 2022, A&A, 665, A106
Alibert, Y., Carron, F., Fortier, A., et al. 2013, A&A, 558, 1
Angerhausen, D., Ottiger, M., Dannert, F., et al. 2023, Astrobiology, 23, 183
Angerhausen, D., Pidhorodetska, D., Leung, M., et al. 2024, AJ, 167, 128
Armstrong, K., Frost, D. J., McCammon, C. A., Rubie, D. C., & Boffa Ballaran, T. 2019, Science, 365, 903
Baraffe, I., Homeier, D., Allard, F., & Chabrier, G. 2015, A&A, 577, A42
Benner, S. A., Bell, E. A., Biondi, E., et al. 2020, ChemSystemsChem, 2, e1900035
Bonati, I., Lichtenberg, T., Bower, D. J., Timpe, M. L., & Quanz, S. P. 2019, A&A, 621, A125
Bonsor, A., Wyatt, M. C., Marino, S., et al. 2023, MNRAS, 526, 3115
Bottrill, A. L., Haigh, M. E., Hole, M. R. A., et al. 2020, ApJ, 895, 141
Boukrouche, R., Lichtenberg, T., & Pierrehumbert, R. T. 2021, ApJ, 919, 130
Bower, D. J., Hakim, K., Sossi, P. A., & Sanan, P. 2022, Planet. Sci. J., 3, 93
Carrión-González, Ó., Kammerer, J., Angerhausen, D., et al. 2023, A&A, 678, A96
Catling, D. C., & Zahnle, K. J. 2020, Sci. Adv., 6, eaax1420
Chao, K.-H., deGraffenried, R., Lach, M., et al. 2021, Chem. Erde/Geochemistry, 81, 125735
Chaverot, G., Turbet, M., Bolmont, E., & Leconte, J. 2022, A&A, 658, A40
Clement, M. S., Kaib, N. A., & Chambers, J. E. 2020, Planet. Sci. J., 1, 18
Clement, M. S., Quintana, E. V., & Quarles, B. L. 2022, ApJ, 928, 91
Cockell, C. S., Simons, M., Castillo-Rogez, J., et al. 2023, Nat. Astron., 8, 675
Dannert, F. A., Ottiger, M., Quanz, S. P., et al. 2022, A&A, 664, A22
Defrère, D., Absil, O., den Hartog, R., Hanot, C., & Stark, C. 2010, A&A, 509, A9
Defrère, D., Hinz, P. M., Kennedy, G. M., et al. 2021, AJ, 161, 186
Dorn, C., & Lichtenberg, T. 2021, ApJ, 922, L4
Elkins-Tanton, L. T. 2012, Annu. Rev. Earth Planet. Sci., 40, 113
Emsenhuber, A., Mordasini, C., Burn, R., et al. 2021, A&A, 656, A69
Ertel, S., Defrère, D., Hinz, P., et al. 2018, AJ, 155, 194
Fortney, J., Robinson, T. D., Domagal-Goldman, S., et al. 2019, Astro2020, 2020, 146
Gaidos, E., Jacobs, T., LaCourse, D., et al. 2019, MNRAS, 488, 4465
Gaidos, E., Mann, A. W., Rojas-Ayala, B., et al. 2022, MNRAS, 514, 1386
Gaillard, F., Bouhifd, M. A., Füri, E., et al. 2021, Space Sci. Rev., 217, 22
Goldblatt, C. 2015, Astrobiology, 15, 362
Goldblatt, C., Robinson, T. D., Zahnle, K. J., & Crisp, D. 2013, Nat. Geosci., 6, 661
Graham, R. J., Lichtenberg, T., Boukrouche, R., & Pierrehumbert, R. T. 2021, psj, 2, 207
Hamano, K., Abe, Y., & Genda, H. 2013, Nature, 497, 607
Hamano, K., Kawahara, H., Abe, Y., Onishi, M., & Hashimoto, G. L. 2015, ApJ, 806, 216
Han, Y., Wyatt, M. C., & Dent, W. R. F. 2023, MNRAS, 519, 3257
Hansen, J. T., & Ireland, M. J. 2022, A&A, 664, A52
Hansen, J. T., Ireland, M. J., & LIFE Collaboration 2022, A&A, 664, A52
Hansen, J. T., Ireland, M. J., Laugier, R., & LIFE Collaboration 2023, A&A, 670, A57
Hirschmann, M. M. 2022, Geochim. Cosmochim. Acta, 328, 221
Hirschmann, M. M. 2023, Earth Planet. Sci. Lett., 619, 118311
Izidoro, A., Bitsch, B., Raymond, S. N., et al. 2021, A&A, 650, A152
Jackson, A. P., & Wyatt, M. C. 2012, MNRAS, 425, 657
Janson, M., Patel, J., Ringqvist, S. C., et al. 2023, A&A, 671, A114
Janssen, L. J., Woitke, P., Herbort, O., et al. 2023, Astron. Nachr., 344, e20230075
Johansen, A., Ronnet, T., Bizzarro, M., et al. 2021, Sci. Adv., 7, eabc0444

Johansen, A., Ronnet, T., Schiller, M., Deng, Z., & Bizzarro, M. 2023, A&A, 671, A75
Kammerer, J., & Quanz, S. P. 2018, A&A, 609, A4
Kammerer, J., Quanz, S. P., Dannert, F., & LIFE Collaboration 2022, A&A, 668, A52
Kane, S. R., Kopparapu, R. K., & Domagal-Goldman, S. D. 2014, ApJ, 794, L5
Kane, S. R., Arney, G., Crisp, D., et al. 2019, J. Geophys. Res. Planets, 124, 2015
Kegerreis, J. A., Teodoro, L. F. A., Eke, V. R., et al. 2018, ApJ, 861, 52
Kegerreis, J. A., Eke, V. R., Catling, D. C., et al. 2020, ApJ, 901, L31
Kempton, E. M. R., & Knutson, H. A. 2024, Rev. Mineral. Geochem., 90, 411
Kempton, E. M. R., Lessard, M., Malik, M., et al. 2023, ApJ, 953, 57
Kennedy, G. M., Wyatt, M. C., Bailey, V., et al. 2015, ApJS, 216, 23
Kenworthy, M., Lock, S., Kennedy, G., et al. 2023, Nature, 622, 251
Konrad, B. S., Alei, E., Quanz, S. P., et al. 2022, A&A, 664, A23
Konrad, B. S., Alei, E., Quanz, S. P., et al. 2023, A&A, 673, A94
Kral, Q., Krivov, A. V., Defrère, D., et al. 2017, Astron. Rev., 13, 69
Kral, Q., Wyatt, M. C., Triaud, A. H. M. J., et al. 2018, MNRAS, 479, 2649
Kral, Q., Matrà, L., Kennedy, G. M., Marino, S., & Wyatt, M. C. 2020, MNRAS, 497, 2811
Krijt, S., Kama, M., McClure, M., et al. 2023, in ASPCS, 534, Astronomical Society of the Pacific Conference Series, 1031
Lambrechts, M., Morbidelli, A., Jacobson, S. A., et al. 2019, A&A, 627, A83
Lammer, H., Scherf, M., Kurokawa, H., et al. 2020, Space Sci. Rev., 216, 74
Lay, O. P. 2004, Appl. Opt., 43, 6100
Lay, O. P. 2006, SPIE, 6268, 62681A
Leconte, J., Forget, F., Charnay, B., Wordsworth, R., & Pottier, A. 2013, Nature, 504, 268
Leconte, J., Forget, F., & Lammer, H. 2015, Exp. Astron., 40, 449
Lichtenberg, T. 2021, ApJ, 914, L4
Lichtenberg, T., & Clement, M. S. 2022, ApJ, 938, L3
Lichtenberg, T., & Miguel, Y. 2024, in Treatise on Geochemistry, 3rd edn.
Lichtenberg, T., Bower, D. J., Hammond, M., et al. 2021, J. Geophys. Res. Planets, 126, e06711
Lichtenberg, T., Schaefer, L. K., Nakajima, M., & Fischer, R. A. 2023, in Astronomical Society of the Pacific Conference Series, 534, Protostars and Planets VII, eds. S. Inutsuka, Y. Aikawa, T. Muto, K. Tomida, & M. Tamura, 907
Lock, S. J., Stewart, S. T., Petaev, M. I., et al. 2018, J. Geophys. Res. Planets, 123, 910
Lock, S. J., Stewart, S. T., & Ćuk, M. 2020, EPSL, 530, 115885
Löhne, T., Krivov, A. V., & Rodmann, J. 2008, ApJ, 673, 1123
Luger, R., & Barnes, R. 2015, Astrobiology, 15, 119
Lupu, R. E., Zahnle, K., Marley, M. S., et al. 2014, ApJ, 784, 27
Mamajek, E. E. 2009, in American Institute of Physics Conference Series, 1158, Exoplanets and Disks: Their Formation and Diversity, eds. T. Usuda, M. Tamura, & M. Ishii (AIP), 3
Mamajek, E. E. 2016, in Young Stars & Planets Near the Sun, 314, eds. J. H. Kastner, B. Stelzer, & S. A. Metchev, 21
Mamajek, E. E., & Meyer, M. R. 2007, ApJ, 668, L175
Matsuo, T., Dannert, F., Laugier, R., et al. 2023, A&A, 678, A97
Meier, T. G., Bower, D. J., Lichtenberg, T., Tackley, P. J., & Demory, B.-O. 2021, ApJ, 908, L48
Meier, T. G., Bower, D. J., Lichtenberg, T., Hammond, M., & Tackley, P. J. 2023, A&A, 678, A29
Miller-Ricci, E., Meyer, M. R., Seager, S., & Elkins-Tanton, L. 2009, ApJ, 704, 770
Morbidelli, A., & Nesvorny, D. 2012, A&A, 546, 1
Olson, P. L., & Sharp, Z. D. 2023, EPSL, 622, 118418
Olson, P., Sharp, Z., & Garai, S. 2022, EPSL, 587, 117537
Ostberg, C. M., Guzewich, S. D., Kane, S. R., et al. 2023, AJ, 166, 199
Owen, J. E., & Mohanty, S. 2016, MNRAS, 459, 4088
Pierrehumbert, R., & Gaidos, E. 2011, ApJ, 734, L13
Piette, A. A. A., Gao, P., Brugman, K., et al. 2023, ApJ, 954, 29
Pluriel, W., Marcq, E., & Turbet, M. 2019, Icarus, 317, 583
Quanz, S. P., Absil, O., Benz, W., et al. 2022a, Exp. Astron., 54, 1197
Quanz, S. P., Ottiger, M., Fontanet, E., et al. 2022b, A&A, 664, A21
Quintana, E. V., Barclay, T., Borucki, W. J., Rowe, J. F., & Chambers, J. E. 2016, ApJ, 821, 126
Ramirez, R. M., & Kaltenegger, L. 2014, ApJ, 797, L25
Ramirez, R. M., & Kaltenegger, L. 2017, ApJ, 837, L4
Reiners, A., Basri, G., & Browning, M. 2009, ApJ, 692, 538
Rojas-Ayala, B., Covey, K. R., Muirhead, P. S., & Lloyd, J. P. 2012, ApJ, 748, 93
Salvador, A., & Samuel, H. 2023, Icarus, 390, 115265
Salvador, A., Massol, H., Davaille, A., et al. 2017, J. Geophys. Res. Planets, 122, 1458
Sasselov, D. D., Grotzinger, J. P., & Sutherland, J. D. 2020, Sci. Adv., 6, eaax3419
Schaefer, L., Wordsworth, R. D., Berta-Thompson, Z., & Sasselov, D. 2016, ApJ, 829, 63

Schlecker, M., Mordasini, C., Emsenhuber, A., et al. 2021a, A&A, 656, A71
Schlecker, M., Pham, D., Burn, R., et al. 2021b, A&A, 656, A73
Schlecker, M., Apai, D., Lichtenberg, T., et al. 2024, Planet Sci., 5, 3
Schlichting, H. E., & Young, E. D. 2022, Planet. Sci. J., 3, 127
Selsis, F., Leconte, J., Turbet, M., Chaverot, G., & Bolmont, É. 2023, Nature, 620, 287
Sleep, N. H., Zahnle, K., & Neuhoff, P. S. 2001, PNAS, 98, 3666
Solomatov, V. 2015, Treatise on Geophysics, 2nd edn., ed. G. Schubert (Elsevier), 81
Stern, S. A. 1994, AJ, 108, 2312
Stökl, A., Dorfi, E., & Lammer, H. 2015, A&A, 576, A87
Su, K. Y. L., Jackson, A. P., Gáspár, A., et al. 2019, AJ, 157, 202
Suer, T.-A., Jackson, C., Grewal, D. S., Dalou, C., & Lichtenberg, T. 2023, Front. Earth Sci., 11, 1159412
Takai, K., Nakamura, K., Toki, T., et al. 2008, PNAS, 105, 10949
Thompson, M. A., Weinberger, A. J., Keller, L. D., Arnold, J. A., & Stark, C. C. 2019, ApJ, 875, 45
Turbet, M., Bolmont, E., Chaverot, G., et al. 2021, Nature, 598, 276
Turbet, M., Ehrenreich, D., Lovis, C., Bolmont, E., & Fauchez, T. 2019, A&A, 628, A12
Vican, L., & Schneider, A. 2014, ApJ, 780, 154
Way, M. J., & Del Genio, A. D. 2020, J. Geophys. Res. Planets, 125, e06276
Williams, C. D., & Mukhopadhyay, S. 2019, Nature, 565, 78
Wordsworth, R., & Kreidberg, L. 2022, ARA&A, 60, 159
Wordsworth, R. D., Schaefer, L. K., & Fischer, R. A. 2018, AJ, 155, 195
Wyatt, M. C., Smith, R., Greaves, J. S., et al. 2007, ApJ, 658, 569
Wyatt, M. C., Kral, Q., & Sinclair, C. A. 2019, MNRAS, 802, 782
Zahnle, K. J., & Carlson, R. W. 2020, in Planetary Astrobiology, eds. V. S. Meadows, G. N. Arney, B. E. Schmidt, & D. J. Des Marais (University of Arizona Press), 3
Zhang, B., & Sigurdsson, S. 2003, ApJ, 596, L95
Zhu, W., & Dong, S. 2021, ARA&A, 59, 291

[1] Kapteyn Astronomical Institute, University of Groningen, PO Box 800, 9700 AV Groningen, The Netherlands
[2] NPP Fellow, NASA Goddard Space Flight Center, Greenbelt, MD, USA
[3] LESIA, Observatoire de Paris, Université PSL, CNRS, Sorbonne Université, Université Paris Cité, 5 place Jules Janssen, 92195 Meudon, France
[4] Institute for Particle Physics and Astrophysics, ETH Zurich, Wolfgang-Pauli-Str. 27, 8093 Zurich, Switzerland
[5] National Center of Competence in Research PlanetS, Switzerland
[6] Institute of Astronomy, KU Leuven, Celestijnenlaan 200D, 3001 Leuven, Belgium
[7] Department of Astronomy and Steward Observatory, The University of Arizona, 933 N Cherry Ave, Tucson, AZ 85721, USA
[8] Large Binocular Telescope Observatory, The University of Arizona, 933 N Cherry Ave, Tucson, AZ 85721, USA
[9] Weltraumforschung und Planetologie, Physikalisches Institut, University of Bern, Gesellschaftsstrasse 6, 3012 Bern, Switzerland Center for Space and Habitability, University of Bern, Gesellschaftsstrasse 6, 3012 Bern, Switzerland
[10] Université Paris-Saclay, Université Paris Cité, CEA, CNRS, AIM, 91191 Gif-sur-Yvette, France
[11] Department of Astrophysics, University of Zurich, Winterthurerstr. 190, 8057 Zurich, Switzerland
[12] Research School of Astronomy and Astrophysics, Australian National University, Canberra 2611, Australia
[13] European Southern Observatory, Karl-Schwarzschild-Straße 2, 85748 Garching, Germany
[14] Centro de Astrobiología (CAB), CSIC-INTA, ESAC campus, Camino Bajo del Castillo s/n, 28692 Villanueva de la Cañada (Madrid), Spain
[15] Department of Astronomy, The University of Michigan, Ann Arbor, MI, USA
[16] Freie Universität Berlin, Institute of Geological Sciences, Berlin, Germany
[17] ETH Zurich, Department of Earth and Planetary Sciences, Sonneggstrasse 5, 8092 Zurich, Switzerland
[18] National Center of Competence in Research "PlanetS", Switzerland
[19] Landessternwarte, Zentrum für Astronomie der Universität Heidelberg, Königstuhl 12, 69117 Heidelberg, Germany

[20] Dept of Physics and Astronomy, York University, 4700 Keele St, Toronto M3J 1P3, Canada

[21] SRON Netherlands Institute for Space Research; Kapteyn Astronomical Institute, University of Groningen, Groningen, Netherlands

[22] Institute of Geochemistry and Petrology, ETH Zurich, Clausiusstrasse 25, 8092 Zurich, Switzerland

[23] Center for Star and Planet Formation, Globe Institute, University of Copenhagen, Øster Voldgade 5–7, 1350 Copenhagen, Denmark

[24] Department of Electronics and Nanoengineering, Aalto University, Espoo, Finland

[25] Department of Physical Sciences, Indian Institute of Science Education and Research Kolkata, Mohanpur 741246, West Bengal, India

[26] School of GeoSciences, University of Edinburgh, Edinburgh EH9 3FF, UK

[27] Centre for Exoplanet Science, University of Edinburgh, Edinburgh EH9 3FD, UK

[28] UK Centre for Astrobiology, School of Physics and Astronomy, University of Edinburgh, Edinburgh, UK

[29] Institute of Astronomy, University of Cambridge, Cambridge, CB3 0HA, UK

[30] Department of Astronomy, University of Michigan, Ann Arbor, MI 48109, USA

[31] Space research & Planetary Sciences (WP), Universität Bern, Gesellschaftsstrasse 6, 3012 Bern, Switzerland

[32] Department of Astrophysics, University of Vienna, Türkenschanzstr. 17, 1180 Vienna, Austria

[33] Universidad de Antofagasta, Antofagasta, Chile

[34] Department of Physics & Astronomy, University of Exeter, Exeter, UK

[35] The University of Tokyo, Astrobiology Center, Tokyo, Japan

[36] Department of Astronomy, Stockholm University, AlbaNova University Center, 10691 Stockholm, Sweden

[37] Globe Institute, University of Copenhagen, Denmark

[38] Centre for Astrophysics Research, University of Hertfordshire, Hatfield, Hertfordshire AL10 9AB, UK

[39] Department of Earth and Planetary Sciences, University of California, Riverside, CA 92521, USA

[40] Lund Observatory, Division of Astrophysics, Department of Physics, Lund University, Box 118, 22100 Lund, Sweden

[41] University of Belgrade, Faculty of Mathematics, Department of astronomy, Studentski trg 16, Belgrade 11000, Serbia

[42] Astrophysics Group, Department of Physics & Astronomy, University of Exeter, Stocker Road, Exeter EX4 4QL, UK

[43] Fakultät für Physik, Universität Duisburg–Essen, Lotharstraße 1, 47057 Duisburg, Germany

[44] Advanced Instrumentation and Technology Centre, Research School of Astronomy and Astrophysics, Australian National University, Canberra, ACT 2611, Australia

[45] Nagoya University, Nagoya, Japan

[46] SRON/Leiden Observatory, Leiden, The Netherlands

[47] SRON Netherlands Institute for Space Research, Leiden, The Netherlands

[48] NOVA Optical Infrared Instrumentation Group at ASTRON, Oude Hoogeveensedijk 4, 7991 PD Dwingeloo, The Netherlands

[49] University of Central Florida, USA

[50] Institut fuer Planetenforschung, DLR, and FU Berlin, Germany

[51] Disruptive Space Technology Centre, RAL Space, STFC-Rutherford Appleton Laboratory, Didcot, UK

[52] Department of Physics & Astronomy, University of Lethbridge, 4401 University Drive, Lethbridge AB, T1K 3M4, Canada

[53] Nicolaus Copernicus Astronomical Center, Polish Academy of Sciences, ul. Bartycka 18, 00-716 Warsaw, Poland

[54] Steward Observatory and Department of Astronomy, The University of Arizona, Tucson, AZ 85721, USA

[55] INAF – Osservatorio Astronomico di Padova, Vicolo dell'Osservatorio 5, 35122, Padova, Italy

[56] Department of Physics and Astronomy, Vanderbilt University, Nashville, TN 37235, USA

[57] School of Engineering and Applied Sciences, Department of Earth and Planetary Sciences, Harvard University, Cambridge, Massachussets, United States of America

Appendix A: Exozodi dust limits

We performed further simulations to study the effect of exozo-diacal dust on LIFE's instrument to a greater extent. These plots are complementary to the ones presented in Sect. 3.5 to present a more complete study on the matter.

Figure A.1 shows the resulting S/N contour plots for shorter integration times in the scenario from Fig. 12 (c), namely a 1500 K planet orbiting a Sun-like star at 1 AU. While Fig. A.4 shows shorter integration times for the planet orbiting an M-dwarf at 0.13 AU, from Fig. 12 (d). Figures A.2-A.3 show the resulting S/N contour plots for the situations displayed respectively in Fig. 12 (a) and (b), with longer integration times. Namely a 700 K planet orbiting both a Sun-like star at 1 AU in Fig. A.2 and an M-dwarf at 0.13 AU in Fig. A.3. The integration times considered are 30, 50, 70, and 100 hours.

G star

For a planet orbiting a Sun-like star detection at the farthest association remains a possibility at thousands of zodis for 5 hours of observation time, as per Fig. A.1 (a). For one hour, Fig. A.1 (b), only β Pictoris remains detectable at a thousand zodis. Nonetheless, TW Hydrae is still detectable for levels of exozodiacal dust of several hundreds. From Fig. A.2 it becomes clear that exozodiacal dust poses a challenge for protoplanets with moderate emission temperatures. β Pictoris becomes detectable at 10^3 zodis after 50 hours, but TW Hydrae is only detected after 100 hours of integration time.
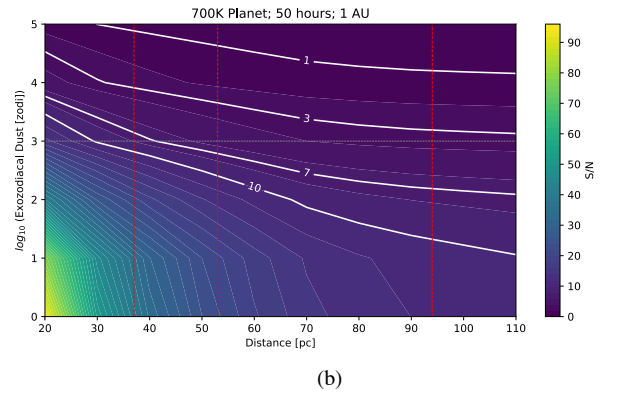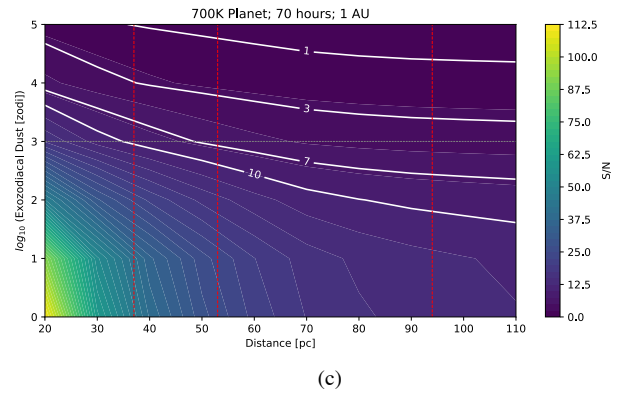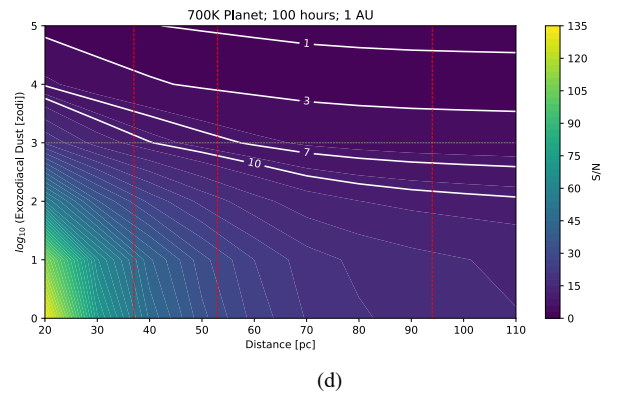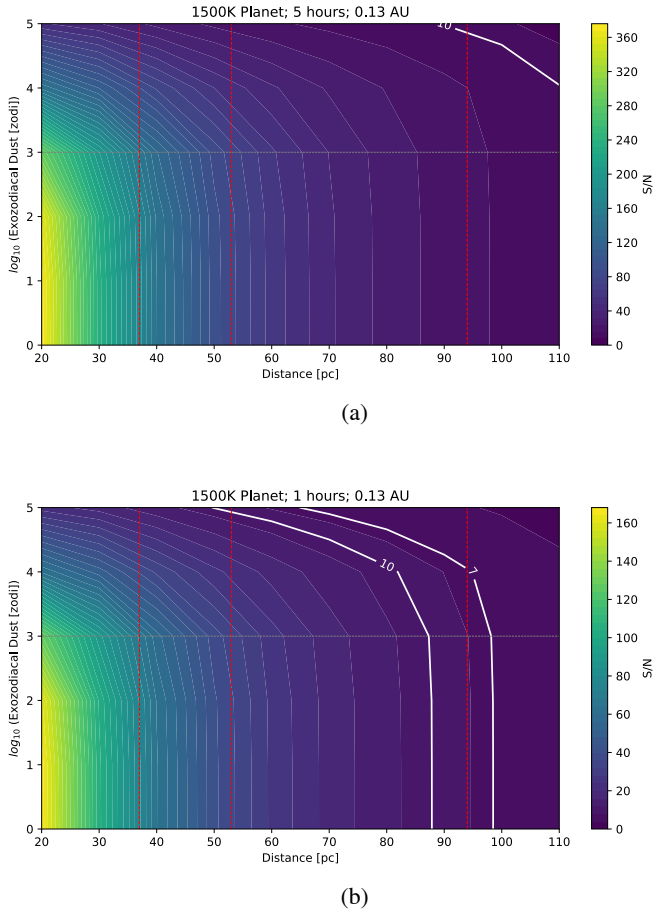

(a)

(b)

(a)

(c)

(b)
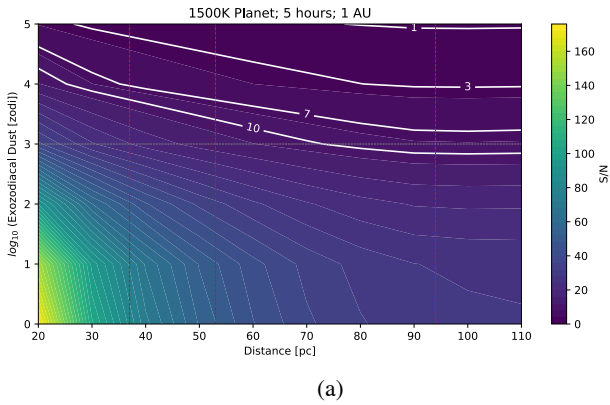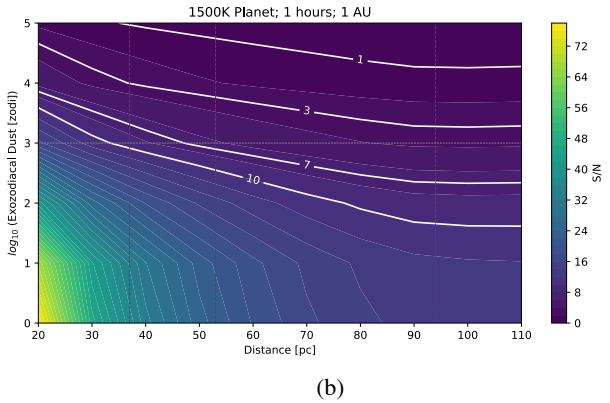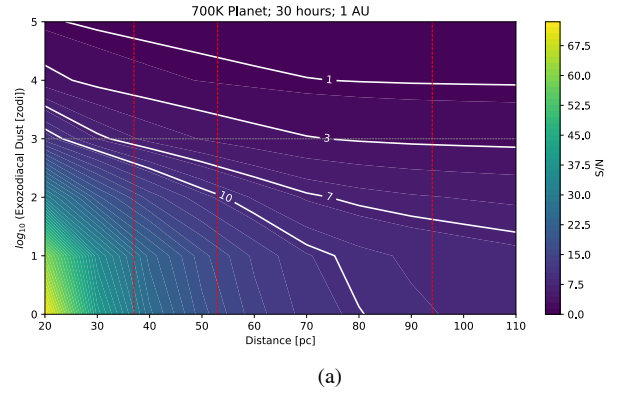
(d)

Fig. A.1: Contour plots of S/N for a 1500 K planet orbiting a Sun-like star at 1 AU for (a) 5 and (b) 1 hour of integration time

Fig. A.2: Contour plots of S/N for a 700 K planet orbiting a Sun-like star at 1AU for (a) 30, (b) 50, (c) 70, and (d) 100 hours of integration time

M-dwarf

The situation for a planet orbiting an M-dwarf star at 0.13 is considerably better than its G-star counterpart. Figure A.3 shows that down to one hour of integration time, a planet in the farthest association η Chamaeleontis is detectable for tens of thousands of zodis. Results from Fig. A.4 show that both β Pictoris and TW Hydrae lie in the detectable region consistently for tens of thousands of zodis, as they were already with 10 hours of integration time. A planet in η Chamaeleontis becomes detectable for a thousand zodis after 100 hours of integration time.

(a)

(b)

Fig. A.3: Contour plots of S/N for a 1500 K planet orbiting an M-dwarf star at 0.13AU for (a) 5 and (b) 1 hours of integration time
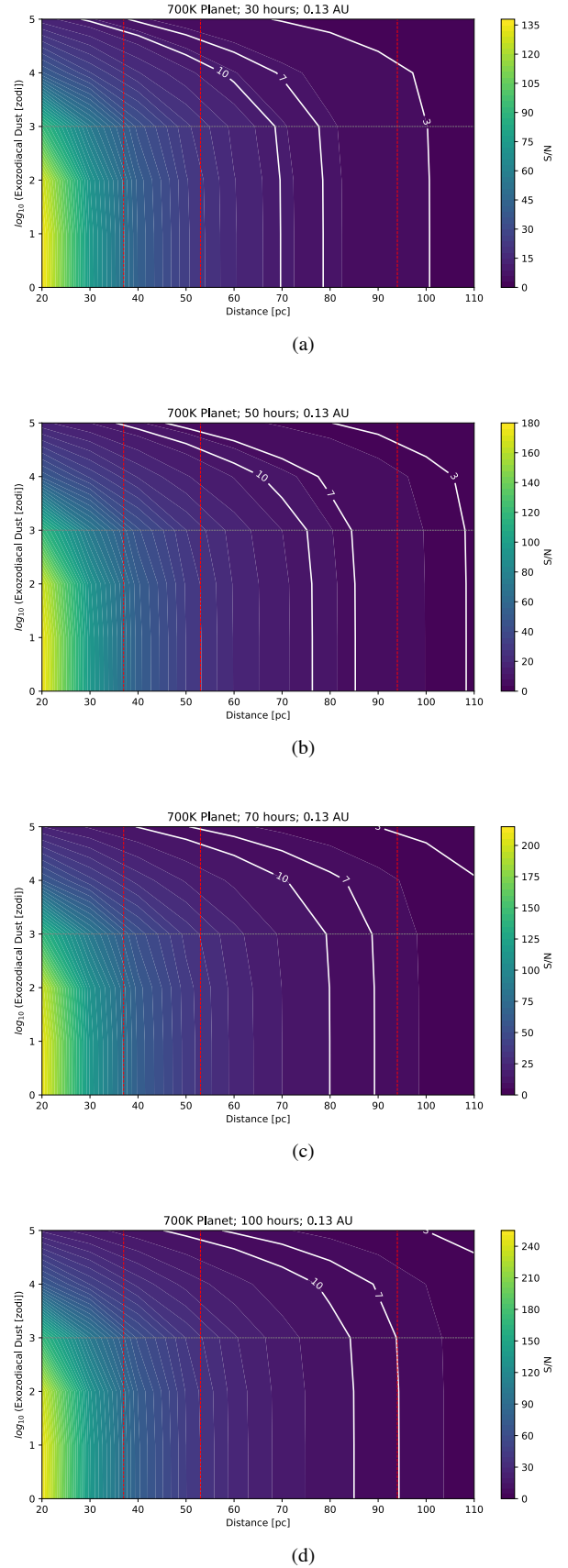

(a)

(b)

(c)

(d)

Fig. A.4: Contour plots of S/N for a 700 K planet orbiting an M-dwarf star at 0.13AU for (a) 30, (b) 50, (c) 70, and (d) 100 hours of integration time

Appendix B: Optimistic throughput

Throughout the simulations in this paper, we kept the photon throughput parameter of the simulator fixed at five percent (see Table 1). This is a relatively pessimistic estimation for the instrument. Therefore it is worth exploring the instrument's performance in constraining the radiating temperature of the observed planet with an optimistic photon throughput of 20%. The following figures are reproductions of Figs. 8-10 respectively. The only difference is the throughput value in the setup of the instrument.

Fig. B.3: Reproduction of Fig. 10 with optimistic 20% photon throughput.

between the considered fluxes (see Fig. B.3) at shorter wavelengths. The peak of the curves in Fig. B.3 reach triple the sigma values for the brighter planet case (1000-700K) than in Fig. 10 and double for the dimmer (400-700K) case. Furthermore, both curves pass the 5σ threshold at longer wavelengths. This means that increasing the photon throughput increases the range of wavelengths useful for constraining radiating temperatures of observed planets.

Similar to these situations, we anticipate all other results presented in the paper to display analogous improvements in detection capability with a more optimistic throughput.
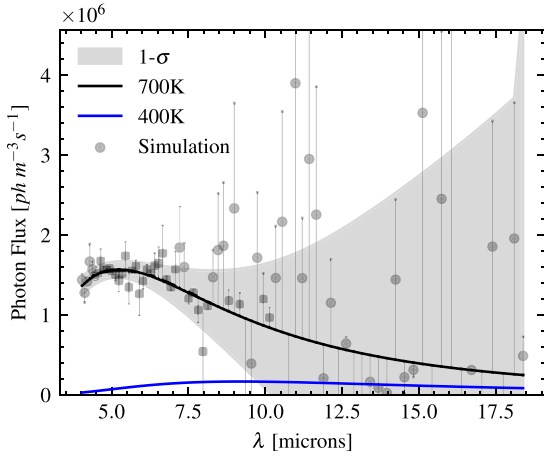

Fig. B.1: Reproduction of Fig. 8 with optimistic 20% photon throughput.
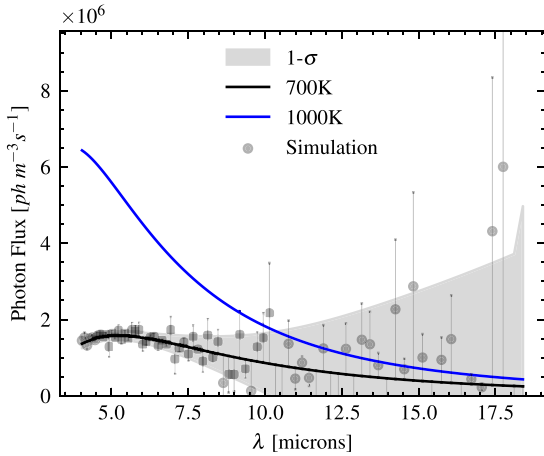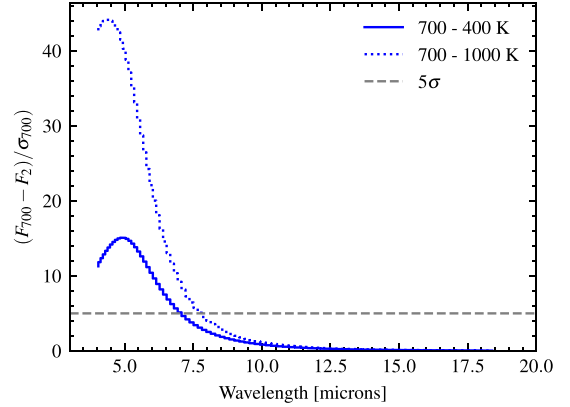

Fig. B.2: Reproduction of Fig. 9 with optimistic 20% photon throughput.

The chances with higher throughput are considerably more optimistic than in Sect. 3.4. In both Fig. B.1 and Fig. B.2 the photon flux of the planet being compared (blue line) reaches the 1-σ uncertainty (shaded) area at longer wavelengths than in their corresponding figures (Figs. 8-9). In the paper, we have already highlighted the importance of shorter wavelengths when observing magma ocean protoplanets with high temperatures ($\gtrsim 1000$K). While longer wavelengths still contain a lot of uncertainty (wide shaded area), the uncertainty is restricted in the shorter wavelength regions. These results show how a greater photon throughput allows for a greater statistical difference